

Commissioning a State-of-Art Small Animal Irradiator and Novel Mini-GRID Treatment  
Technique

by

Simon Brundage

Graduate Program in Medical Physics  
Duke University

Date: \_\_\_\_\_

Approved:

\_\_\_\_\_  
Mark Oldham, Supervisor

\_\_\_\_\_  
Yvonne Mowery

\_\_\_\_\_  
Greg Palmer

Thesis submitted in partial fulfillment of  
the requirements for the degree of Master of Science in the Graduate Program in  
Medical Physics in the Graduate School  
of Duke University

2022

ABSTRACT

Commissioning a State-of-Art Small Animal Irradiator and Novel Mini-GRID Treatment  
Technique

by

Simon Brundage

Graduate Program in Medical Physics  
Duke University

Date: \_\_\_\_\_

Approved:

\_\_\_\_\_  
Mark Oldham, Supervisor

\_\_\_\_\_  
Yvonne Mowery

\_\_\_\_\_  
Greg Palmer

An abstract of a thesis submitted in partial  
fulfillment of the requirements for the degree  
of Master of Science in the Graduate Program in  
Medical Physics in the Graduate School of  
Duke University

2022

Copyright by  
Simon Brundage  
2022

## Abstract

**Purpose:** To validate commissioning results associated with the Xstrahl Small Animal Radiation Research Platform (SARRP) installed at Duke University in October 2021, verify the accuracy of the Xstrahl Point Dose Calculator (PDC) and MuriPlan dose calculation in simple geometries, and design and characterize a novel in-house kV mini-GRID capability on the SARRP.

**Methods:** After installation at Duke University, Xstrahl SARRP TG-61 output was measured for independent verification using a Farmer ion chamber at reference conditions (33 cm SSD, 2 cm depth, open field, 220 kVp, 13 mA). Half-value layer was measured using the same ion chamber, with copper sheets to vary thickness. The accuracy of the PDC was investigated in simple water and bolus stack phantoms using EBT3 film. A range of field sizes (10x10, 20x20, 30x30, 40x40, 10x20, 20x10, 15x40, 10x40, 30x70 mm<sup>2</sup>) and depths (1 cm, 2 cm) were spot-checked. MuriPlan simulations of treatment delivery to the bolus phantom and water phantom were compared to results of EBT3 film measurements. Metal Oxide Semiconductor Field Effect Transistor (MOSFET) detectors were also used for independent verification, with detectors being embedded within a tissue-equivalent mouse phantom at 1 cm depth. GRID irradiations were performed with the SARRP, using a 220 kVp beam, 13 mA, and a 40 mm x 40 mm field size. Pencil and bar GRIDs with beamlet spacings of 1 mm and 1.25 mm were characterized by first inserting GRID into a 3D-printed mount and positioning the mount on top of a PLA plastic block, surrounded by distilled water. EBT3 films were

infix to the top level of the PLA block and positioned at isocenter. PDC was utilized to determine irradiation time. The beam was turned on for 102 seconds—sufficient time to administer 6 Gy with a 40 mm x 40 mm field size to the surface film at isocenter with no GRID blocking the beam. EBT3 film results were analyzed to determine the output factors, peak-to-valley ratios, integral dose relative to open field, relative dose maps, as well as to produce dose volume histograms for each GRID. Results were compared to GRID characterizations in Johnson *et al* [18]. GRID characterizations were used to inform experimental plan for pre-clinical trial evaluating treatment efficacy of GRID therapy with PD-L1 checkpoint inhibition compared to conventional radiation therapy.

**Results:** TG-61 dose rate and half-value layer measured during on-site commissioning showed excellent agreement with Xstrahl factory commissioning results ( $\approx$  1% difference). The PDC and MuriPlan dose calculation predicted results for field sizes and depths demonstrated acceptable agreement with actual results measured by EBT3 film (.2% to 12%), with exception of several outliers. Using EBT3 film dosimetry for verification (tissue-equivalent bolus medium), MuriPlan simulations were within 2% and 12% difference from the film measured dose for 5/7 field sizes in the bolus phantom and within 3% and 13% for 4/5 field sizes in the water phantom. MOSFET detector measurements using the mouse phantom demonstrated improved agreement with the PDC-predicted dose, with percent errors ranging from .12% to 5.97% (with a single outlier at 18.3%). Measured output factors using the SARRP for the 20 mm x 20 mm pencil GRIDs were  $.77 \pm .03$  and  $.74 \pm .02$  (1 mm and 1.25 mm beamlet spacing, respectively). For the bar GRIDs, these values were evaluated to be  $.83 \pm .03$  and  $.80 \pm$

.03 (1 mm and 1.25 mm beamlet spacing, respectively). Peak:valley ratios for the 1 mm and 1.25 mm beamlet spacing pencil GRIDs were determined to be  $24.5 \pm 0.6$  and  $25.1 \pm 1.3$ , respectively. Peak:valley ratios for the 1 mm and 1.25 mm beamlet spacing bar GRIDs were found to be lower than for pencil GRIDs with equivalent beamlet spacing, being evaluated to be  $13.2 \pm 1.1$  and  $18.5 \pm 1.2$ , respectively. Output factors, peak:valley ratios, integral dose relative to open field, and dose volume histograms for the pencil and bar GRIDs using the SARRP largely corroborated the results of Johnson *et al* in terms of experimental trends (peak:valley ratios being higher for pencil GRIDs and increasing with increasing beamlet spacing, output factors decreasing with increasing beamlet spacing for both GRID types, and decreasing integral dose with increasing beamlet spacing for pencil GRIDs and increasing integral dose with increasing beamlet spacing for bar GRIDs). 4.67% to 30.5% difference was observed for experimentally measured peak:valley ratios relative to the results for the same GRIDs in Johnson *et al*. Better agreement was demonstrated in GRID output factor measurements ( $\approx 0\%$  to 14%). Integral dose experimental measurements demonstrated exceptional agreement with Johnson *et al*., with percent differences ranging from 1% to 2.1%. These measured differences are likely a result of using the SARRP versus the XRAD 225Cx used in Johnson *et al*, but lend significant credence to reproducibility of results found using the XRAD 225Cx.

**Conclusions:** The PDC and MuriPlan computations provide an effective estimate of the exposure time necessary to deliver dose for corresponding MVC field sizes and depths (within 6% error using the MOSFET for verification). EBT3 film was determined to be an

unreliable measure of SARRP dose delivery; MOSFET detectors demonstrated more consistency and effectiveness for treatment planning verification. Xstrahl's SARRP was able to replicate the kV mini-GRID capabilities of the XRAD 225Cx used in Johnson *et al.* and can be used for mini-GRID characterizations and preclinical mouse trials.

# Contents

Abstract .....	iv
List of Tables.....	ixi
List of Figures .....	xi
Acknowledgements .....	xii
1. Introduction.....	1
1.1 Xstrahl Small Animal Radiation Research Platform.....	1
1.1.1 Technical Specification.....	1
1.1.2 Cone Beam Computed Tomography Imaging .....	5
1.1.3 Dosimetric Commissioning Procedure.....	6
1.1.4 MuriPlan Integrated Point Dose Calculator.....	7
1.1.5 MuriPlan Treatment Planning Software.....	8
1.2 Spatially Fractionated Radiation Therapy Background and Theory .....	9
1.2.1 Biological Mechanisms of Spatially Fractionated Radiation Therapy... 10	
1.2.1.1 Bystander Effects.....	10
1.2.1.2 Abscopal Effects .....	11
1.2.2 GRID Therapy .....	12
1.2.2.1 Normal Tissue Sparing and Immune Response .....	12
1.2.2.2 Clinical Applications of GRID Therapy.....	13
1.2.2.3 Preceding GRID Therapy Research at Duke University .....	15
1.3 Project Scope.....	17
2. Methods .....	19
2.1 Verifying Xstrahl Factory Commissioning Results.....	19
2.1.1 Measurement and Verification Tools.....	19
2.1.1.1 Farmer Ion Chamber .....	19
2.1.2 Measurement and Verification Setup .....	20
2.1.2.1 Task Group-61 Output Measurement.....	20
2.1.2.2 Half-Value Layer.....	21
2.2 Verifying the Accuracy of the MuriPlan Integrated Point Dose Calculator .....	23
2.2.1 Measurement and Verification Tools.....	24
2.2.1.1 EBT3 Gafchromic Film .....	24

2.2.1.2	Metal Oxide Semiconductor Field Effect Transistor Detectors .....	27
2.2.1.3	MuriPlan Treatment Planning Software Simulation .....	29
2.2.2	Measurement and Verification Setup .....	30
2.2.2.1	Water Phantom Spot-Check Measurements .....	31
2.2.2.2	Bolus Phantom Spot-Check Measurements .....	32
2.2.2.3	Mouse Phantom Spot-Check Measurements .....	33
2.3	Reproducing kV Mini-GRID Evaluation Methods using the XRAD 225Cx Small Animal Irradiator with the SARRP .....	34
2.3.1	GRID Mount .....	35
2.3.1.1	Table Mount.....	35
2.4	GRID Manufacturing and Design .....	36
2.4.1	Material .....	37
2.4.2	Beamlet Pattern and Spacing.....	38
2.4.2.1	Pencil GRID .....	38
2.4.2.2	Bar GRID .....	39
2.5	GRID Characterizations.....	40
2.5.1	Peak-to-Valley Ratio .....	41
2.5.2	Output Factor .....	42
2.5.3	Dose Map .....	43
2.5.3.1	Dose Volume Histogram.....	43
2.5.3.2	Integral Dose Relative to Open Field .....	43
3.	Results.....	45
3.1	Verifying Xstrahl Factory Commissioning Results.....	45
3.1.1	TG-61 Output Measurement .....	45
3.1.2	Half-Value Layer.....	46
3.2	Verifying the Accuracy of the MuriPlan Integrated Point Dose Calculator .....	47
3.2.1	Water Phantom Spot-Check Measurements .....	47
3.2.2	Bolus Phantom Spot-Check Measurements .....	49
3.2.3	Mouse Phantom Spot-Check Measurements .....	53
3.2.4	MuriPlan Simulations.....	54
3.3	GRID Characterizations.....	58
3.3.1	Peak-to-Valley Ratio .....	58

3.3.2 Output Factor .....	60
3.3.3 Dose Map .....	61
3.3.3.1 Dose Volume Histogram.....	63
3.3.3.2 Integral Dose Relative to Open Field .....	67
4. Conclusions .....	69
4.1 Verifying Xstrahl Factory Commissioning Results.....	69
4.2 Verifying the Accuracy of the MuriPlan Integrated Point Dose Calculator .....	69
4.3 GRID Characterizations.....	70
4.4 Future Study .....	72
References .....	74

## List of Tables

Table 1: Components of SARRP Pro Package .....	1
Table 2: Manufacturer SARRP Output Verification Data .....	7
Table 3: Preclinical Workflow using MuriPlan Treatment Planning Software .....	8
Table 4: Scanner Settings for EBT3 Film Dosimetry .....	25
Table 5: EBT3 Film Image Processing Workflow.....	27
Table 6: SARRP TG-61 Output Calculation Table .....	45
Table 7: Comparison of Manufacturer and Experimentally Measured TG-61 Output.....	45
Table 8: Comparison of Manufacturer and Experimentally Measured Half-Value Layer .....	47
Table 9: Water Phantom Measurements for PDC Verification.....	48
Table 10: First Bolus Phantom Measurements for PDC Verification.....	50
Table 11: Second Bolus Phantom Measurements for PDC Verification.....	52
Table 12: Mouse Phantom Measurements for PDC Verification.....	53
Table 13: Comparison of Bolus Phantom EBT3 Film Results and MuriPlan Simulations. .....	55
Table 14: Comparison of Water Phantom EBT3 Film Results and MuriPlan Simulations. .....	56
Table 15: Comparison of Expected and Measured Peak:Valley Ratios.....	59
Table 16: Comparison of Expected and Measured Output Factors .....	60
Table 17: Comparison of Expected and Measured Integral Doses Relative to Open Field .....	67

# List of Figures

Figure 1: Xstrahl SARRP Pro System [2].....	2
Figure 2: Xstrahl Motorized Variable Collimator [1] .....	4
Figure 3: CBCT Imaging Geometries [3].....	5
Figure 4: MuriSlice User Interface [1] and SARRP Laser Alignment .....	6
Figure 5: Observed Bystander Effect Mechanism [11].....	11
Figure 6: Commercially Available GRID Block [5] .....	14
Figure 7: Farmer Ion Chamber .....	21
Figure 8: Half-Value Layer Measurement Setup .....	23
Figure 9: EBT3 Film Pre-Scan Orientation.....	26
Figure 10: EBT3 Film Post-Scan Orientation .....	26
Figure 11: MOSFET Detector Design [22].....	28
Figure 12: MuriPlan Treatment Planning Software Interface .....	29
Figure 13: Water Phantom for PDC Verification.....	31
Figure 14: Bolus Phantom for PDC Verification.....	33
Figure 15: MOSFET Calibration and PDC Verification Setup .....	34
Figure 16: Table Mount Setup for GRID Characterizations .....	36
Figure 17: Mini-GRIDs used for Characterizations [18] .....	37
Figure 18: Experimental Pencil GRIDs used .....	39
Figure 19: Experimental Bar GRIDs used.....	40
Figure 20: Point-Dose Calculator Interface used for GRID Characterization Exposure Time .....	41
Figure 21: Line Profile Example for Calculating Peak:Valley Ratio .....	42
Figure 22: Half-Value Layer Measurement Plot.....	46
Figure 23: Water Phantom Calibration Curve .....	48
Figure 24: Bolus Phantom Calibration Curve 1 .....	49
Figure 25: Bolus Phantom Calibration Curve 2 .....	51
Figure 26: GRID Characterization Calibration Curve (Water Phantom) .....	58
Figure 27: Comparison of Expected and Measured Relative Dose Maps (Pencil GRIDs). .....	61
Figure 28: Comparison of Expected and Measured Relative Dose Maps (Bar GRIDs) ....	62

Figure 29: Comparison of Expected and Measured Dose-Volume Histograms (Pencil  
GRIDs) ..... 64

Figure 30: Comparison of Expected and Measured Dose-Volume Histograms (Bar  
GRIDs) ..... 66

## **Acknowledgements**

I would like to acknowledge and thank the following individuals for their support of this work, as well as of myself, on a personal level: Dr. Mark Oldham; Dr. Gregory Palmer; Dr. Yvonne Mowery; Timothy Johnson; Patrick Sansone; Breylon Riley; my parents, Trenton and Karen Brundage; my brothers, Hayden and Sawyer Brundage; and, finally, my partner, Carol Moreno.

# 1. Introduction

## 1.1 *Xstrahl Small Animal Radiation Research Platform*

The Xstrahl Small Animal Radiation Research Platform (SARRP) is a multi-modality image guided irradiator—installed, radiation protection surveyed, and acceptance tested at Duke University on October 27th, 2021. Functionally, the system consolidates cone beam computed tomography (CBCT) technology with the capabilities of a small animal irradiation platform designed for pre-clinical trials. The SARRP is innovative insofar as the system replicates the radiosurgery capabilities of a clinical linear accelerator, including delivery of radiation from any angle and variable collimation.

### 1.1.1 Technical Specification

The SARRP package included the following components:

**Table 1: Components of SARRP Pro as provided in the Xstrahl SARRP technical description [1].**

225 kV Dual Focused X-Ray Tube	X-Ray Detector Panel
SARRP X-Ray Controller	Electronic Portal Imaging Device
SARRP User Interface and PC	X-Ray Generator and Cooling System
Safety Interlock Circuit	Peripheral Camera/Alignment Lasers
Robotic Specimen Stage	Standard Accessories Kit
Integrated Lead Shielding	Targeting Accuracy: .2 mm

SARRP has an X-ray energy range of up to 225 kVp, with an accompanying range of 0 to 30 mA and 3.2 kW maximum power. This 225 kV dual focused X-Ray tube is mounted to a motorized gantry, complete with a 360° range of motion [1]. The X-Ray tube assembly is composed of a unipolar tube with a cooled anode at ground potential, as well as a high voltage receptacle. The irradiation system itself is encapsulated by a self-shielded enclosure, with dimensions 205 cm x 148 cm x 104 cm height, width, and depth, respectively. This self-shielding capability enables the SARRP to be stored in proximity to laboratory animals.



**Figure 1: Xstrahl SARRP Pro System adjacent to remote X-Ray Controller (MP1) and SARRP control software [2].**

Similar to other small animal irradiators, the SARRP utilizes two different filters for treatment and imaging: .15 mm copper filtration for treatment, and aluminum filtration for imaging—with .8 mm beryllium filtration inherent to each setting. These different filters fundamentally modify the beam spectra to fit either

imaging or treatment applications, changing both the effective energy and output of the beam. The presence of these filters is integral to proper functionality of the SARRP. For example, if the imaging filter (aluminum) was to be utilized for a 220 kVp beam, the effective energy of the beam would be lower than expected, as less lower energy photons would be attenuated by the filter. Consequently, not only would there be increased scatter (collimator and phantom), but also higher dose in superficial tissue layers relative to the predicted dose distribution—with the added potential of inducing skin toxicity if treating small animals.

The SARRP platform is controlled remotely via a user interface software. From this interface, the user can acquire a CBCT for the purposes of target localization, reposition the stage manually using x, y, and z inputs, and customize irradiation and imaging setups. The SARRP software is enhanced by its utilization of Xstrahl's treatment planning software (TPS), MuriPlan, and additional research accessories. This includes the Xstrahl Motorized Variable Collimator (MVC), used for expedient adjustment of field size for experimental use.

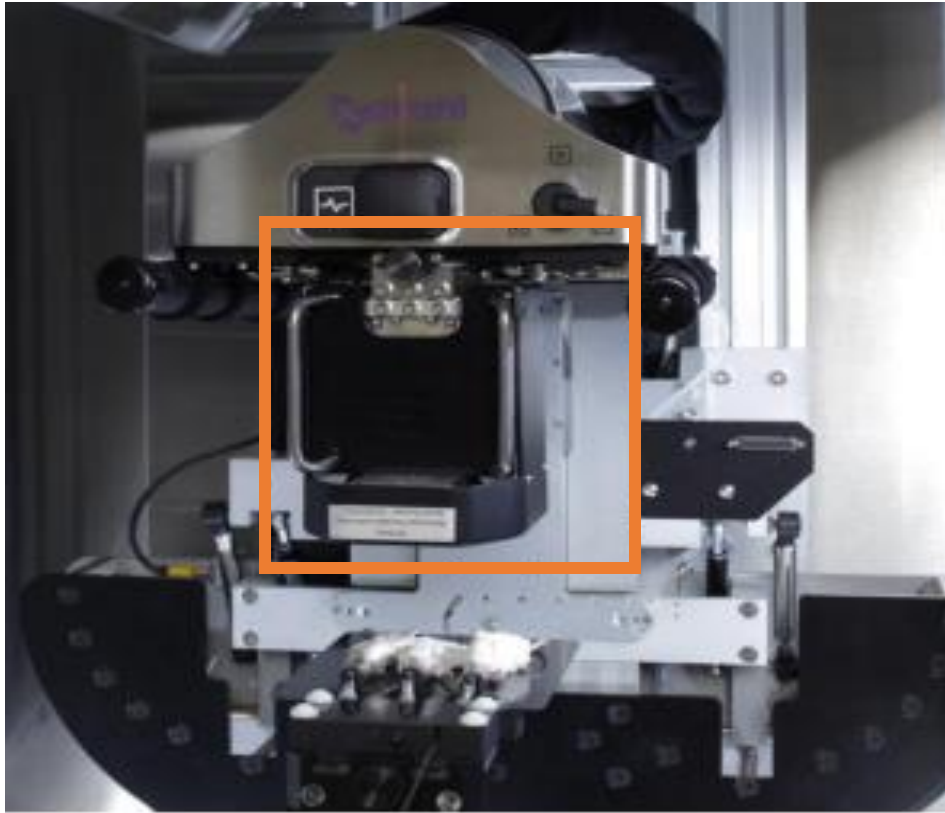


**Figure 2: Xstrahl Motorized Variable Collimator, boxed in orange [1].**

As an improvement to standard fixed collimators, Xstrahl's MVC provides an effective range of collimation settings, with field sizes as small as 1 mm x 1 mm, and as large as 40 mm x 80 mm. These field sizes are defined at the machine isocenter, at 35 cm source-to-surface distance (SSD). Composed of two sets of tungsten jaws (X1, Y1, X2, Y2), the collimator rotates to maintain alignment with the beam—allowing for a reduction of radiation penumbra [1].

In addition to CBCT imaging, the SARRP also includes the option of fluoroscopic X-ray portal imaging for use prior or during treatment. This portal camera is situated within the gantry, providing a beam's eye view of the central axis. Notably, the SAARP user interface allows for live 2D images to be captured during treatment, as well.

## 1.1.2 Cone Beam Computed Tomography Imaging

CT imaging with the SARRP uses a cesium iodide scintillator coupled with an amorphous silicon receptor to produce high-resolution images. This operation is performed with the gantry starting position being opposite to the plane of the detector (rotated 90°), enabling the use of a pancake geometry to rotate the specimen of interest in front of the detector. The predefined imaging settings include low-energy X-Rays (60 kV, 0.8 mA) and a small focal spot (1.0 mm) for acquiring the CBCT. These settings are conducive to minimal imaging dose (1 cGy to 3 cGy).

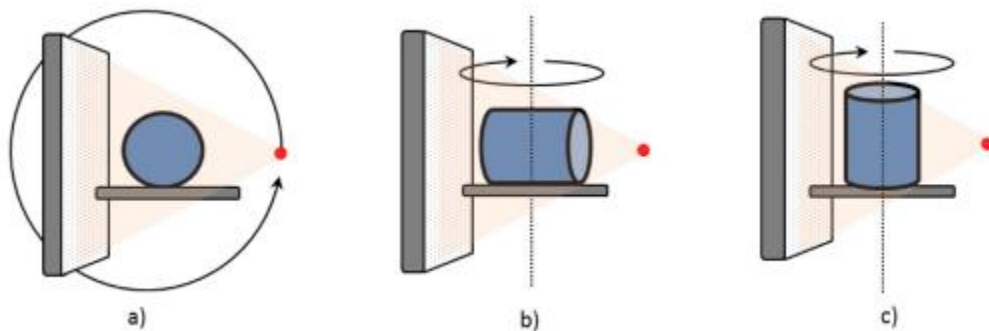


**Figure 3: (a) Conventional CBCT imaging geometry. (b) Pancake CBCT imaging geometry. (c) Phantom standing up in conventional geometry [3].**

67 seconds are required for a complete CBCT acquisition. This imaging time includes a 360° scan, as well as the use of the Feldkamp-Davis-Kress (FDK) image reconstruction algorithm. The minimum possible voxel size for FDK reconstruction using the SARRP is 10  $\mu m$ , with the potential for user modulation of voxel size. Additionally, the operator can adjust the number of projections for CBCT

acquisition, with an increasing number of projections corresponding to increasing spatial resolution.

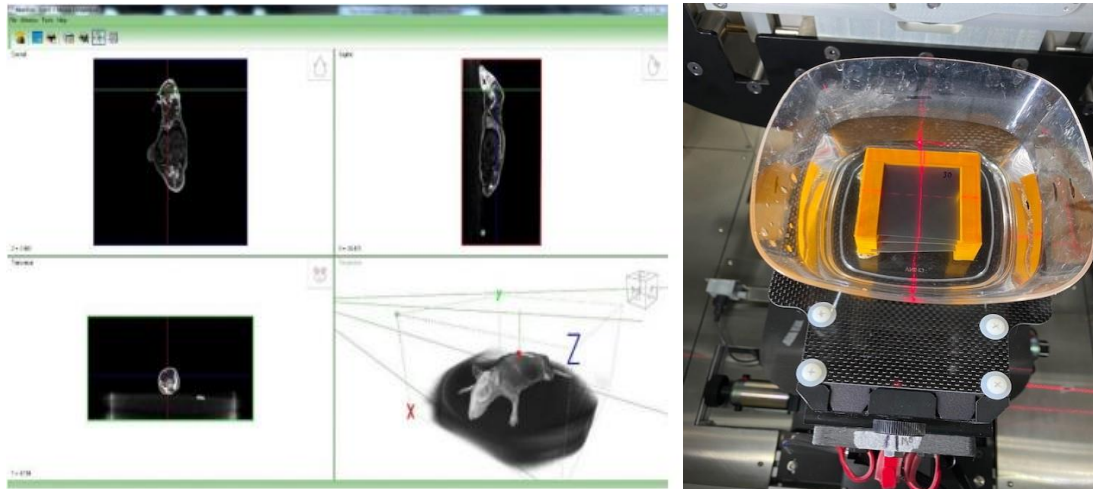


**Figure 4: MuriSlice user interface with capability of manually selecting isocenter using acquired CBCT image [1] (left) and SARRP horizontal, longitudinal, and lateral lasers aligned at isocenter on EBT3 film in water phantom (right).**

Following CBCT acquisition, isocenter coordinates can be established in MuriSlice and used to move the stage to the required treatment position. The isocenter is marked by three lasers (horizontal, longitudinal, lateral) mounted within the SARRP frame.

### **1.1.3 Dosimetric Commissioning Procedure**

Dosimetric commissioning of the SARRP was completed on September 8<sup>th</sup>, 2021, by Xstrahl, following a three-stage process [3]:

- I. Determination of SARRP output using large field reference conditions and calibrated ion chamber and electrometer
- II. Calibration of EBT films for absolute dose using output measurement setup conditions

III. Full therapeutic dose characterization using 2D-cross-plane profiles for the complete set of therapeutic collimators over a range of SSDs

Xstrahl used a PTW TN30013 farmer ionization chamber to determine that the dose rate, or output, was 3.6575 Gy/min at 2 cm depth. 8 EBT films were subsequently used to measure the dose to water using different exposure times and were validated with the dose based on nominal output. The results of this dose verification are displayed in the table below:

**Table 2: SARRP output verification conducted by Xstrahl on September 8<sup>th</sup>, 2021, using EBT film at 33 cm SSD, 2 cm depth in solid water phantom, open field, .15 mm Cu filter, 220 kVp, 13 mA. Exposure times were calculated using the nominal output determined using farmer chamber (3.6575 Gy/min).**

Target Dose (cGy)	Ideal Exposure Time (s)	Delivered Exposure Time (s)	Mraw_Ave over two measurements (nC)	Meas'd Dose to Water (cGy)	Dose Based on Nominal Output (cGy)	Ramp-Up Error (%)	Film Number (#)
0	0.00	0	0.000	0.00	1.24	N/A	1
20	3.28	3	3.539	19.51	19.53	-0.08	2
40	6.56	7	7.965	43.91	43.91	0.00	3
80	13.12	13	14.595	80.47	80.49	-0.02	4
160	26.25	26	28.970	159.72	159.73	0.00	5
320	52.50	53	58.835	324.38	324.32	0.02	6
640	104.99	105	116.300	641.21	641.30	-0.01	7
960	159.49	157	173.900	958.78	958.28	0.05	8

### 1.1.4 MuriPlan Integrated Point Dose Calculator

The MuriPlan Integrated Point Dose Calculator (PDC) enables the operator to calculate an exposure time consistent with user-inputted parameters. These parameters include depth (mm), dose (cGy), gantry angle, and either the fixed collimator or MVC field size (mm), depending on the irradiation setup.

Computations to acquire exposure time are performed using the operator’s preference of the convolution/superposition or Monte Carlo dose calculation algorithm.

### 1.1.5 MuriPlan Treatment Planning Software

MuriPlan is an integrated TPS for the Xstrahl SARRP, functioning to allow the operator to acquire or load a CBCT reconstructed image and subsequently devise a treatment plan. This software, like the SARRP, replicates clinical functions such as image registration, contouring, establishing beam angles or arcs, as well as providing important analytical information for treatment evaluation such as dose volume histograms and isodose lines over the user-defined contours.

**Table 3: Traditional pre-clinical experimentation workflow using the MuriPlan treatment planning software [1].**

1. CT Acquisition	2. Multi-Modality Image Fusion	3. Simple Segmentation
4. Contouring	5. Beam Planning	6. Dose Computation
7. Verification	8. Delivery	9. Reporting

MuriPlan enables the operator to run simulations of the prescribed treatment using the acquired CBCT reconstructed image. This element of MuriPlan exists as an analog to dose calculation and treatment simulation in a standard clinical TPS. Additionally, as with the PDC, MuriPlan simulations can utilize either the convolution/superposition or Monte Carlo dose calculation algorithm to compute the dose, produce dose-volume histograms, and display consequent isodose lines.

## **1.2 Spatially Fractionated Radiation Therapy Background and Theory**

Spatially Fractionated Radiation Therapy (SFRT) is an application of external beam radiation therapy (EBRT) involving treatment of the total tumor with non-uniform dose—concurrently delivering the prescribed dose to the target volume while also adhering to normal tissue tolerances [5]. SFRT was first explored as a means of mitigating skin injury associated with low energy X-rays by Alban Köhler [5]. In the early 1900s, radiation treatments used low energy X-rays; consequently, a perforated block (composed of attenuating material like lead or bronze) divided into smaller fields was used to preserve normal tissue in blocked regions of the X-ray beam. Not only did this approach reduce dose to valuable basal cells in the skin, but these blocks—each effectively containing an array of pencil beams—were found to not impact the dose distribution at deeper tissue levels [6].

With the inception of megavoltage (MV) scale radiation treatment modalities in the 1950s, these blocks became less practical, as skin sparing effects could be achieved with relative simplicity compared to with orthovoltage X-rays. Despite this, certain SFRT experimental regimens have retained relevance to clinical practice, including GRID therapy, ultra-high dose rate (FLASH) radiotherapy, minibeam radiation therapy (MRT), and LATTICE radiotherapy (LRT). These regimens highlight the potential for therapeutic index improvement using SFRT, provided that continued research is done exploring the radiobiological mechanisms of SFRT, as well as on optimizing target coverage and normal tissue sparing [6].

## **1.2.1 Biological Mechanisms of Spatially Fractionated Radiation Therapy**

While SFRT has been practiced clinically for a century, there is limited understanding of the underpinnings of SFRT tumor control [6]. As previously mentioned, orthovoltage X-ray beams were utilized until the 1950s, and while there has been considerable study on the radiobiology of SFRT, the specific biological mechanisms remain ambiguous. Existing *in vitro* and *in vivo* evidence supports the theory of radiation-induced signaling effects between cells, including bystander and abscopal effects [6, 7, 8].

### **1.2.1.1 Bystander Effects**

Bystander effects are defined as radiobiological signals delivered by irradiated cells to unirradiated cells within the area of treatment. It has been observed that cell irradiation using SFRT stimulates the release of cytokines; these cytokines induce chromosomal methylation, which ultimately results in either DNA damage or cellular apoptosis [9]. This notion was validated by a 2012 study conducted by Asur *et al.*, demonstrating that “significant bystander killing of cells adjacent to the...irradiated region” can occur in SFRT conditions [10].

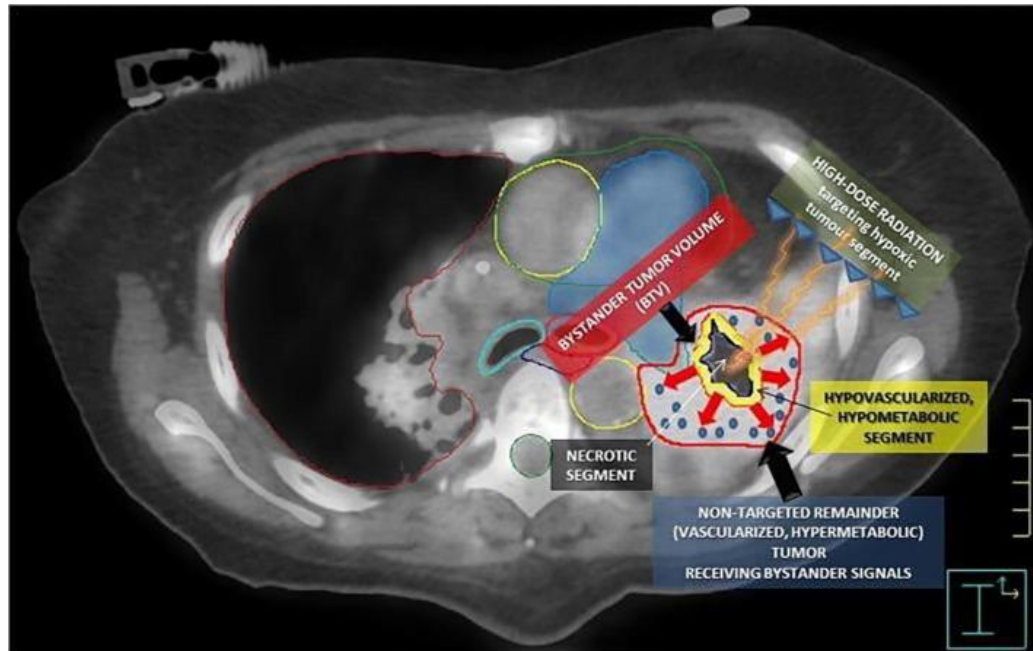


**Figure 5: Observed bystander effect biological mechanism for Stereotactic Body Radiation Therapy – Partial Tumor Irradiation Targeting Hypoxic Segment of Bulky Tumors (SBRT-PATHY) [11]. Red arrows represent “anti-angiogenic bystander signal[s]” released by the irradiated tumor.**

### 1.2.1.2 Abscopal Effects

Abscopal effects describe radiobiological signals delivered by irradiated cells to unirradiated cells in locations outside of the treatment area. The induction of abscopal effects is predicated on the release of “tumor antigens and damage-associated molecular pattern[s]” by irradiated tumor cells, and the subsequent activation of adaptive immunity through increased presence of antigen-presenting cells and lymphocytes [11].

A number of clinical cases have demonstrated the synergetic effectiveness of radiotherapy coupled with immunotherapy, suggesting that radiation-induced abscopal effects function as an *in situ* vaccination [12]. This *in situ* vaccination effect involves the exiting of “antigen-educated T cells” from the irradiated region, and the

detection of tumor antigens in distant regions of the body. Optimally, this process leads to regression of metastases outside of the local region-of-interest (ROI).

## **1.2.2 GRID Therapy**

GRID therapy is an SFRT treatment approach where a physical block—typically made of lead, bronze, or Cerrobend—with a variable number and style of perforated openings is placed in the path of the beam. In doing so, as is characteristic of SFRT, a significant portion of the target tumor volume remains unirradiated after treatment.

### **1.2.2.1 Normal Tissue Sparing and Immune Response**

Markovsky *et al.* provided substantial evidence that partial irradiation of a tumor volume was not only sufficient for tumor control, but also a mechanism for sparing normal tissue and promoting an overall immune response [13]. In this study, 67NR murine orthotopic breast tumors—in both immunocompetent and non-immunocompetent (nude) mice—were irradiated with full irradiation or hemi-irradiation using a 2 cm x 2 cm collimator on a microirradiator. The results of this experiment demonstrated that a “significant increase in CD8+ T cells occurred in the nonirradiated portion of the hemi-irradiated tumors 24 hours post-RT,” in addition to immunostimulation via abscopal effects in the collateral tumor. These abscopal effects were induced without the presence of PD-L1 checkpoint inhibitors, and when the murine immune system was inhibited (using the Lewis lung carcinoma (LLC) tumor model—an immunogenic tumor), the efficacy of partial irradiation tumor control was largely diminished.

The implications of this work provide credence to the immunostimulatory potential of partial tumor irradiation—namely, GRID therapy. Coupled with results like those provided in Sammer *et al.*, where it was evidenced that minibeam techniques are conducive to higher tissue dose tolerance, the optimization potential for GRID therapy as a means of normal tissue sparing and tumor control (both local and distant) becomes quite clear [14].

#### **1.2.2.2 Clinical Applications of GRID Therapy**

Modern GRID therapy applications using MV-scale beams were first used in the early 1990s, seeking to achieve palliative debulking of large, radioresistant tumors, or as a boost procedure to conventional radiation therapy [15]. Clinical GRID therapy uses one of three methods to create the GRID-pattern radiation fluence for treatment: the aforementioned physical GRID block, a software generated virtual GRID block, or use of multi-leaf collimator (MLC) modulation [6].

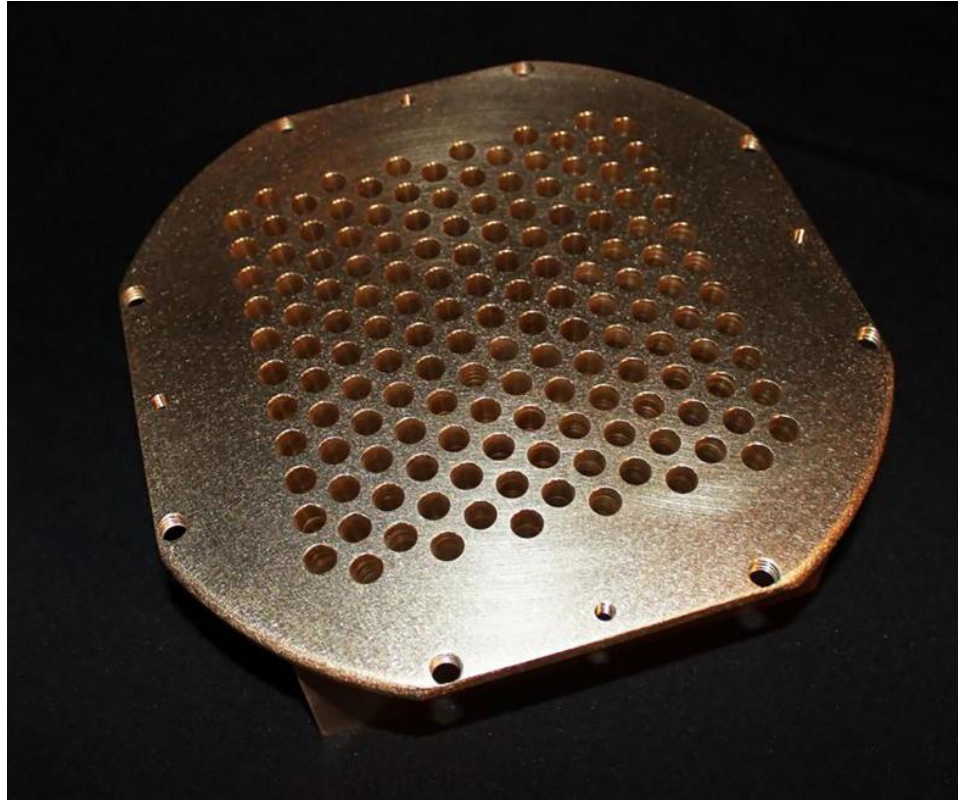


**Figure 6: Commercially available GRID block, manufactured by decimal, LLC [5]. Beamlets are milled in a manner that passage will follow beam divergence. Pictured GRID has a 50:50 open to closed blocked area ratio with the blocked regions being composed of an attenuating alloy material.**

A case study was done comparing the effectiveness of a physical brass GRID versus that of an analogous MLC-based GRID for a patient with stage IV head and neck squamous cell carcinoma. The patient was treated with a single fraction of 15.0 Gy prescribed to a point centered on the tumor volume, underneath the central axis hole of the GRID compensator [16]. This was subsequently followed by 5 fractions of conformal beams, each delivering 6 Gy, in both cases. It was found that the MLC-based GRIDs require far more MUs than the physical GRID block (529% more), which has significant implications for the clinical environment. Indeed, reducing the number of MUs required for treatment suggests less time that the patient is required

to be immobilized for treatment. While this does not mean that MLC-based GRIDs are infeasible in the clinical environment, it does affirm that physical GRIDs will likely retain their clinical utility in the future.

For GRID therapy, an issue with implementation concerns deep-seated, bulky tumors; these tumors require high treatment dose using conventional GRID therapy, implying a higher dose also delivered to normal tissue [5]. A key motivation for GRID therapy research involves optimizing the physical GRIDs to reduce dose to normal tissue, while concurrently delivering the optimal dose to the deep-seated tumor. 3D LRT was developed specifically to address this complication, using localized high-dose vertices with defined separation from one another (similar to 2D GRID therapy) in a 3D arrangement to improve tumor control without exacerbating normal tissue toxicity levels [17].

### **1.2.2.3 Preceding GRID Therapy Research at Duke University**

This thesis is predicated on the work of Johnson *et al.* at Duke University, where kV pencil and bar GRIDs were manufactured, characterized, and implemented into a pre-clinical mice trial to evaluate the treatment efficacy of GRID therapy compared to conventional radiation therapy using the XRAD 225Cx small animal irradiator [18]. This work involved the precision milling of 3 mm thick lead pencil and bar GRIDs, and the subsequent characterization of these GRIDs using metrics such as output factor, peak-to-valley ratio, and features of the dose distribution. These characterizations were completed using EBT3 film dosimetry.

The bar GRID with 1.00 mm beamlet spacing was used in the pre-clinical trial, where C57BL/6 mice were transplanted with p53/MCA soft-tissue sarcoma. Mice received a single fraction of 15 Gy to the ROI through three separate treatment arms: conventional irradiation of the total tumor volume, hemi-irradiation like in Markovsky *et al.*, and GRID therapy. An additional treatment arm was included for the control, where mice remained unirradiated. This study exists as the first to compare GRID therapy versus conventional radiation therapy as the primary treatment (not as a boost).

The results of Johnson *et al.* demonstrated that kV GRIDs can achieve much higher peak-to-valley ratios than MV GRIDs used clinically. It also evidenced that GRID therapy and hemi-irradiation were not able to achieve the same level of local tumor control that conventional radiation therapy was able to achieve. With these results, it was decided that future research steps would involve evaluating the treatment efficacy of GRID therapy coupled with an immunostimulatory treatment (such as a PD-L1 checkpoint inhibitor) compared to conventional radiation therapy. This preclinical trial would also utilize a pencil GRID, as opposed to a bar GRID, for its relatively high peak-to-valley ratio and normal tissue sparing effects compared to other GRIDs.

### **1.3 Project Scope**

Xstrahl's dosimetric commissioning process provides reliable data regarding the output of the SARRP. However, with the GRID characterizations and GRID preclinical trial in Johnson *et al.* being completed using the XRAD 225Cx small animal irradiator, methodological changes were examined to account for use of the newly installed SARRP. This investigation ensures continuity between the work of Johnson *et al.* and future GRID therapy research at Duke University. As such, this thesis seeks to accomplish three primary aims:

- I. To validate Xstrahl factory commissioning results regarding the TG-61 output and half-value layer associated with the SARRP. These measurements assure that the nominal output is consistent with dosimetric commissioning results and can be utilized for subsequent verification steps.
- II. To verify the accuracy of the MuriPlan Integrated Point Dose Calculator and treatment planning software for varying depths and field sizes using the nominal output of the SARRP. Once verified, MuriPlan can be used with certainty by the operator at Duke University for experimental use—specifically, in this case, for GRID characterizations and preclinical trial treatment planning.
- III. To adapt the methodology for GRID characterizations from the XRAD 225Cx small animal irradiator to the Xstrahl SARRP, perform GRID characterizations (including output factor, peak-to-valley ratio, dose map) for 20 mm x 20 mm pencil and bar GRIDs, and to cross-reference the results of

these characterizations with Johnson *et al.* This methodology can be adapted and utilized for future GRID characterizations and mouse irradiations using mini-GRID therapy techniques with the SARRP.

## **2. Methods**

### **2.1 Verifying Xstrahl Factory Commissioning Results**

Two primary measurements were used to validate the factory commissioning results of the Xstrahl SARRP: TG-61 output and half-value layer (HVL). The TG-61 output measurement ensures consistency with the measured nominal output provided by Xstrahl, allowing for use of the SARRP output at 2 cm depth for validation of the MuriPlan PDC. Xstrahl dosimetric commissioning included a TG-61 output measurement, where the result was determined to be 3.6575 Gy/min.

Functionally, the half-value layer measurement is an indirect evaluation of beam quality and intensity; in this particular case, it serves as a validation of photon beam energy. For the 220 kVp, 13 mA beam setting used by the SARRP, the manufacturer determined half-value layer was .67 mm Cu.

#### **2.1.1 Measurement and Verification Tools**

Output and half-value layer measurements were completed using a Farmer ion chamber. A solid water phantom was provided by Xstrahl for TG-61 output measurement, and copper sheets were used to vary the thickness to determine the half-value layer for the SARRP 220 kVp beam.

##### **2.1.1.1 Farmer Ion Chamber**

The PTW TN30010 was the farmer chamber model used for verification of dosimetric commissioning data. With a nominal energy range of 30 kV to 50 MV, the farmer chamber is optimal for dosimetry measurements associated with the Xstrahl

SARRP. Farmer chambers are effective at absolute photon dosimetry for field sizes between 5 cm x 5 cm and 40 cm x 40 cm. Since both measurements were conducted with an open field, field size limitations of the farmer chamber were assumed negligible.

## 2.1.2 Measurement and Verification Setup

Both the TG-61 output measurement and half-value layer were completed at 220 kVp, 13 mA, and using an open field. Results were analyzed using Microsoft Excel.

### 2.1.2.1 Task Group-61 Output Measurement

The American Association of Physicists in Medicine's (AAPM) TG-61 protocol was used to evaluate the dose rate at 2 cm depth for the Xstrahl SARRP. To measure TG-61 output, the PTW 30010 farmer chamber was inserted into a solid water phantom at 2 cm depth, using an open field, 220 kVp, 13 mA, 33 cm SSD, and using a .15 mm copper filter. Exposure time used for TG-61 was 1 minute. Final output measurement was the average of 3 individual measurements. The TG-61 dose rate equation was utilized:

$$\dot{D}_w = \frac{MN_k P_Q P_S [(\frac{\mu_{en}}{\rho})_{air}^w]_{water}}{t + \delta t} \quad (Eq. 1)$$

where M is the corrected chamber reading,  $N_k$  is the ion chamber calibration factor,  $P_Q P_S$  is the chamber correction factor, t is the total radiation time, and  $\delta t$  is the end effect. The corrected chamber reading included a temperature-pressure correction factor. Measured temperature and pressure was 20° Celsius and 101.32 kPa,

respectively. Temperature and pressure were corrected to match standard environmental conditions of temperature (22° Celsius, 101.33 kPa) using this temperature-pressure correction factor, calculated using the following equation:

$$P_{TP} = \frac{273.2 + T}{273.2 + 22.0} * \frac{101.33}{P} \quad (Eq.2)$$

where T and P are defined as the measured temperature and pressure at the time of measurement.

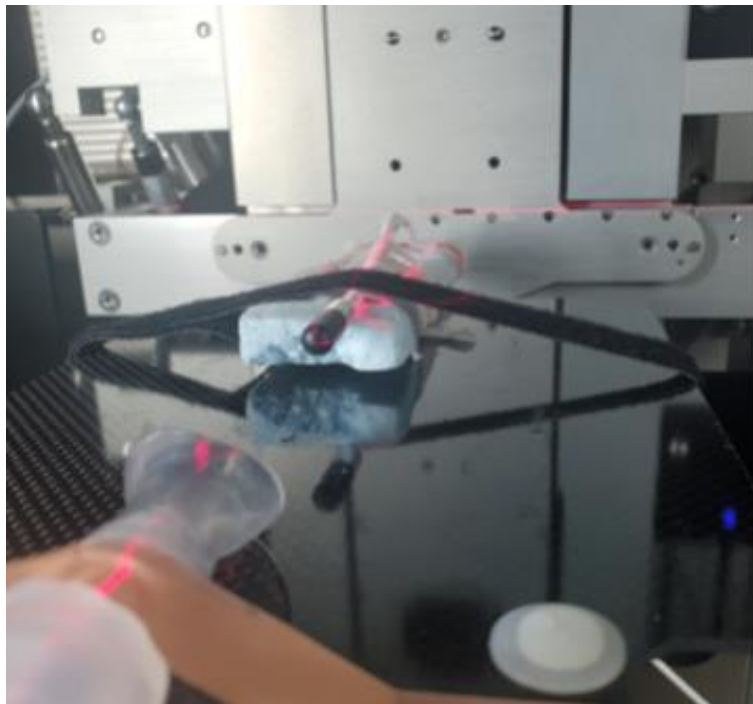


**Figure 7: Farmer ion chamber used for TG-61 output verification. Pictured setup was not used for output measurement.**

#### **2.1.2.2 Half-Value Layer**

The half-value layer measurement was setup by taping the farmer chamber to a foam block, meant to bolster the chamber to a position level with where the stage would be for conventional treatment. The MVC was removed prior to irradiations, enabling the use of an open field in addition to output measurement

conditions including 220 kVp, 13 mA, and an intrinsic .15 mm copper filter used for treatment (the SARRP uses an aluminum filter for imaging).

Two measurements were taken for each thickness of copper, with each measurement exposure time being 60 seconds. Copper sheets (.05 to .1 mm thickness) were taped to the gantry, with additional copper sheets being attached after each measurement. Thickness of copper measured included 0 mm, .25 mm, .35 mm, .45 mm, .5 mm, .6 mm, .65 mm, .7 mm, and 1 mm. Half-value layer data was fitted to an exponential decay plot of the following form:

$$I = I_0 e^{-\mu x} \quad (\text{Eq. 3})$$

where  $I_0$  is the initial charge reading using the farmer chamber with no copper taped to the gantry (open field),  $\mu$  is the linear attenuation coefficient,  $x$  is the thickness of copper, and  $I$  is the charge reading after variable attenuation.

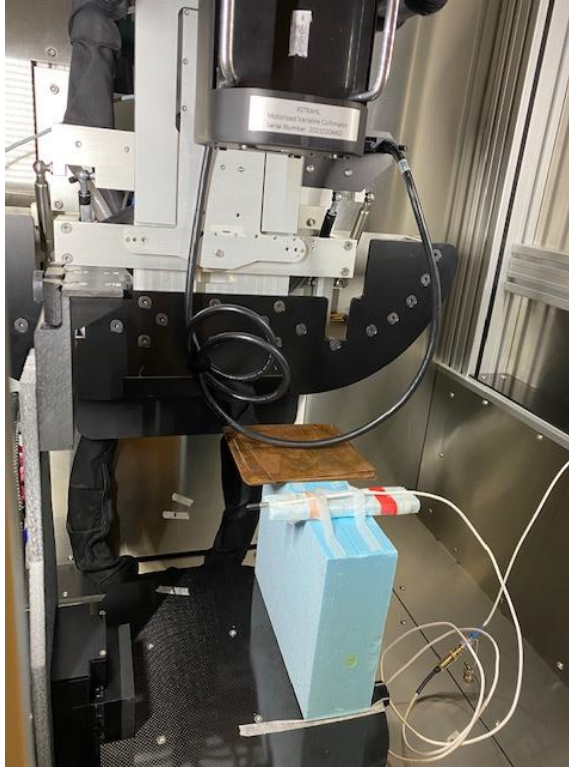


**Figure 8: Half-value layer measurement setup for commissioning results validation. Sheets of copper with varying thickness (pictured) were taped to the gantry. MVC was removed.**

## ***2.2 Verifying the Accuracy of the MuriPlan Integrated Point Dose Calculator***

The MuriPlan PDC calculates the exposure time necessary to deliver the prescribed dose by the operator. For the purposes of preclinical experimentation using the SARRP, it was determined that independent verification of the accuracy of the PDC was necessary. This included varying depth and MVC field size over a number of measurements spanning three different mediums.

As previously mentioned, the MuriPlan PDC has two dose computation options: convolution/superposition and Monte-Carlo dose calculation algorithm. Of

these two options, the convolution/superposition algorithm was used for calculating exposure times. The Monte-Carlo algorithm requires considerably more time to compute relative to the convolution/superposition algorithm, making it less practical for regular use.

## **2.2.1 Measurement and Verification Tools**

Three different verification methods were employed to validate the PDC. Multiple modalities were used due to the inherent uncertainty associated with EBT3 film. Since the SARRP is to be used for preclinical experiments, it was deemed necessary to independently verify film measurements with metal oxide semiconductor field effect transistor detectors (MOSFETs), as well as by using MuriPlan treatment planning simulations to check for discrepancies between the predicted and actual film dosimetry results.

### **2.2.1.1 EBT3 Gafchromic Film**

EBT3 Gafchromic film was used for relative dosimetry measurements to validate the PDC. Film dosimetry is optimal because of its superior spatial resolution, convenience for 2D dosimetry, and near tissue equivalence [19]. EBT3 film was preferred to EBT2 film due to its symmetric construction, with the point of measurement being set in the center of the film. In addition, as a dosimetry technique, EBT3 film has the advantage of improved performance in the dose range of .2 to 10 Gy; for the purposes of this thesis, all doses delivered fall between 2 Gy and 6 Gy [20]. This made EBT3 film a viable tool for PDC dose verification.

Despite having advantages, however, there remains a degree of volatility associated with film measurements using small animal irradiators, which often operate in the energy range of 200 to 300 keV. While there is minimal response difference for EBT3 film when photon beam energy is above 100 keV, the average energy of the SARRP beam is approximately 75 keV. As such, it is plausible the energy dependence of EBT3 film could impact the results of this experiment.

Steps were taken to reduce the level of uncertainty associated with EBT3 film measurements, including the creation of new calibration curves on each measurement day; unique calibration curves for different mediums (water, bolus); and, finally, multiple measurements were taken for each calibration curve point. These steps were taken in addition to more conventional, tested methods such as handling film with gloves, storing film in dark envelopes, and reducing exposure to ultraviolet (UV) light.

Pre-scans and post-scans of EBT3 film were completed using the following scanner settings on an Epson 11000XL scanner:

**Table 4: Scanner settings used for EBT3 film dosimetry to verify MuriPlan PDC. These same settings were also used for the GRID characterizations. 200 DPI resolution can be used instead of 400, if necessary – 400 DPI was selected for enhanced image quality for smaller field sizes and the millimeter-sized beams associated with GRID therapy.**

Mode: Photo mode	Image type: 48-bit color	Image format: TIFF
Document source: Transparency unit	Resolution: 400 DPI	Color management: none
Document type: Color positive film	Scanning quality: high	Auto exposure: off

Films were allowed at minimum 24 hours to develop post-irradiation, being placed on the scanner in an identical orientation to how they were placed during the pre-scans. The scanner was cleaned prior to pre-scans and post-scans, and films were only handled using their edges for placement on the scanner. Each film was spaced approximately 5 mm from those directly adjacent to them. Two scans were taken per grouping of EBT3 film, and pixel intensities were averaged. Scanner was given 20 minutes of warm-up time prior to both pre-scans and post-scans being performed [21].

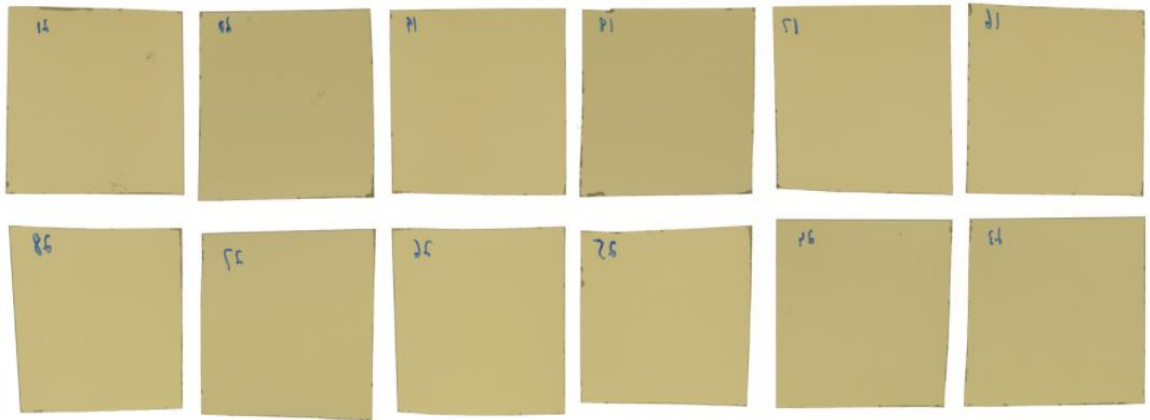


**Figure 9: Example of pre-scan orientation of EBT3 film for validation of MuriPlan PDC.**

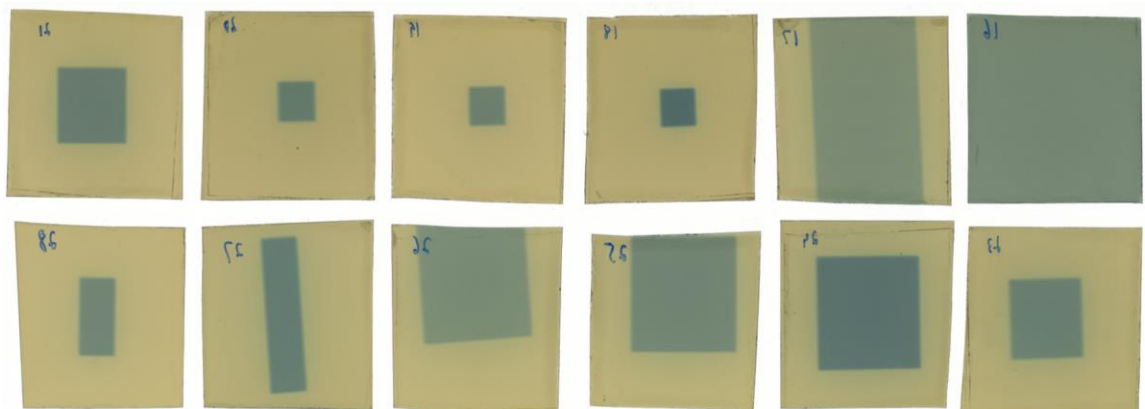


**Figure 10: Example of post-scan orientation of EBT3 film for validation of MuriPlan PDC.**

Film analysis is predicated on evaluating the change in optical density from the pre-scans of the film to the post-scans. This evaluation was completed using the following equation:

$$\Delta OD = \log_{10} \left( \frac{I_{pre-scan}}{I_{post-scan}} \right) \quad (Eq. 4)$$

, with  $I_{pre-scan}$  representing the pixel intensity during the pre-scans, and  $I_{post-scan}$  being defined as the pixel intensity during the post-scans.

Image processing was completed using ImageJ, with the following workflow:

**Table 5: Image processing workflow utilized for analyzing the results of EBT3 film dosimetry.**

1. TIFF files are opened in ImageJ
2. Color channels are split in ImageJ, with the red image channel being used for analysis
3. ROI manager is used to draw a circular ROI for each film
4. Each ROI is measured, with key values such as the mean pixel intensity and standard deviation of pixel intensities being saved
5. Data is imported into Microsoft Excel
6. Calibration curve is created using data imported into Excel, with the x-axis representing the change in optical density, and the y-axis corresponding to absorbed dose
7. Calibration data is fit to a 3 <sup>rd</sup> degree polynomial [21]
8. Calibration curve is used to determine dose delivered to EBT3 film

### 2.2.1.2 Metal Oxide Semiconductor Field Effect Transistor Detectors

MOSFET detectors are semiconductor-based dosimeters, often utilized for small field dosimetry, in-vivo dosimetry, and profile measurements [22]. As a verification modality, they were selected for this experiment due to their effectiveness at small field dosimetry, given that the MVC field sizes range from 2

mm x 2 mm to 40 mm x 80 mm. When positioned within a mouse phantom at 1 cm depth, it was determined that MOSFET detectors create a practical environment for reliably verifying the PDC.

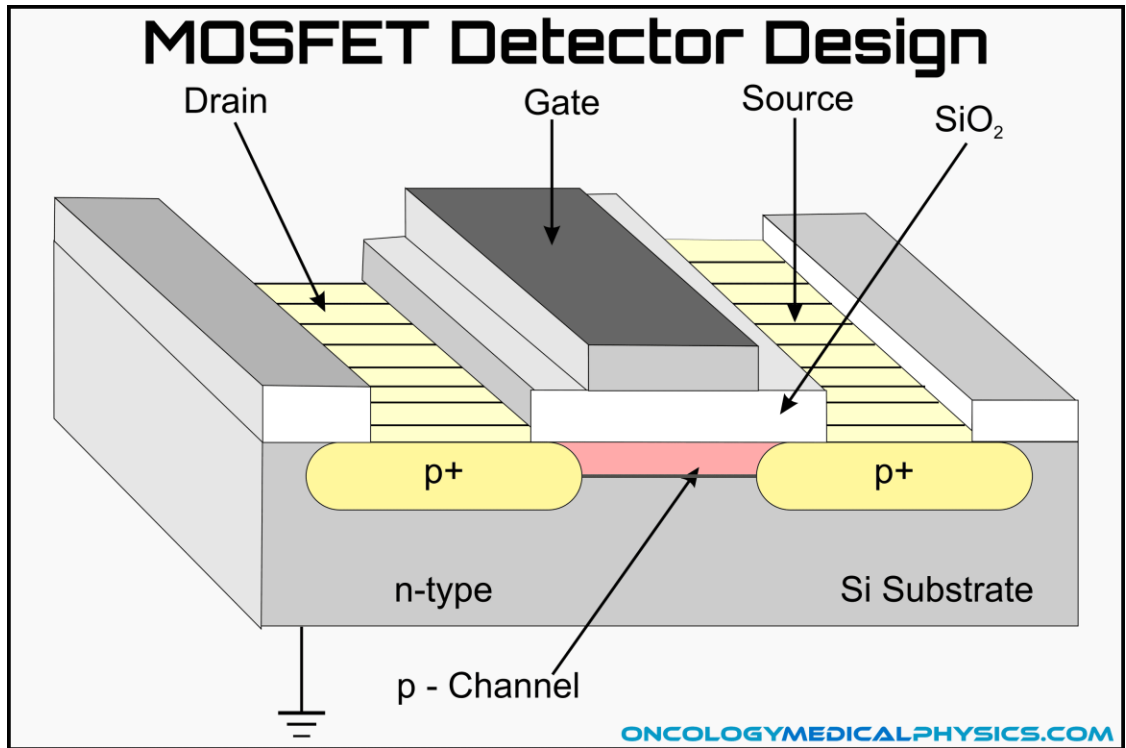


**Figure 11: Schematic of a MOSFET detector, illustrating key features such as the drain, gate, source, and silicon dioxide insulation [22]. The pictured MOSFET (p-channel) is the most common version and was utilized to verify the PDC.**

Functionally, MOSFET detectors determine dose via a four step process:

electron-hole pairs are created in the silicon dioxide insulation post-irradiation;

electron-holes migrate to the region between the substrate and insulation; voltage is

applied to the gate to induce current flow between the source and the drain; and,

once current flow has been achieved, the corresponding change in threshold voltage

is assumed to be proportional to the number of electron-holes created, allowing for

measurement of dose [22].

MOSFET detectors often have an effective lifespan of approximately 100 Gy due to the build-up of “trap filling,” or, rather, the filling of valence bands in the insulation. Consequently, for extended experimentation, often multiple MOSFET detectors must be used, each with their own calibration factor. Two MOSFET detectors were used to complete measurements to verify the PDC.

### 2.2.1.3 MuriPlan Treatment Planning Software Simulation

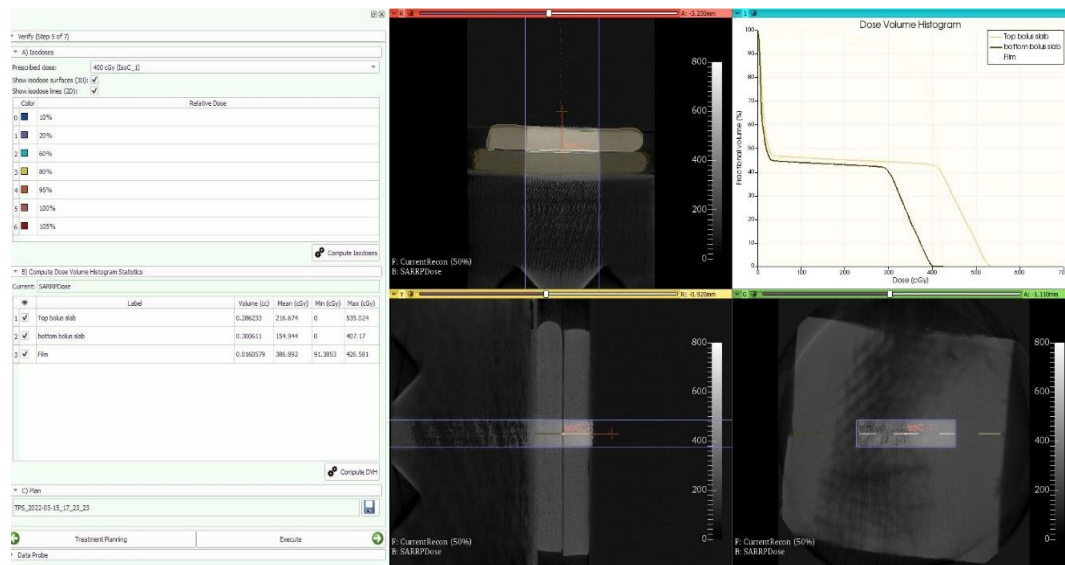


**Figure 12: MuriPlan treatment planning software interface, used to prescribe 400 cGy to 1 cm depth in the 2 cm bolus stack. Displayed also are MuriPlan generated dose-volume histograms, CT data showing a static AP beam targeted at a delineated isocenter at 1 cm depth (where the film is situated), as well as contours of the two bolus slabs and film in the center.**

Like the PDC, the MuriPlan treatment planning software uses the operator’s preference of the convolution/superposition or Monte Carlo dose calculation algorithm. As previously mentioned, MuriPlan simulations were used to validate the results of the film EBT3 film dosimetry. This was done for the bolus phantom, as evidenced in Figure 12, as well as the water phantom, with treatment of 400 cGy being prescribed to 1 cm depth and 300 cGy being prescribed to 2 cm depth,

respectively. CBCT images of the bolus and water phantoms were used in MuriPlan to provide CT data for the simulations.

Once simulation results were acquired, they were cross-referenced with the results of the film dosimetry, with percent difference being calculated for the results associated with each film tested MVC field size.

### **2.2.2 Measurement and Verification Setup**

Three different verification setups were used to verify PDC exposure time estimates, involving three mediums (water, bolus, tissue-equivalent mouse phantom) and two verification modalities (EBT3 film, MOSFET detectors). Multiple setups were used for several reasons: to optimize the EBT3 film calibration curve and PDC verification setup; to determine the optimal medium for GRID characterizations; and, finally, to replicate a simple mouse experimental setup using a mouse phantom.

Since the nominal output was measured to be approximately 3.66 Gy/min at 2 cm depth, films were placed at 2 cm depth to create EBT3 film calibration curves for both the water and bolus stack. The nominal TG-61 output value was used to compute the requisite exposure time to deliver 1 Gy, 2 Gy, 3 Gy, 4 Gy, 4.5 Gy, and 5 Gy to different films placed at 2 cm depth in these phantoms; these films were used to create an EBT3 film calibration curve for the water and bolus phantoms. The PDC was subsequently used to calculate the exposure time necessary to deliver 3 Gy to films at 2 cm depth in the water phantom, and 4 Gy to 1 cm depth in the bolus phantom using MVC field sizes including 10x10, 20x20, 30x30, 40x40, 10x20, 20x10,

15x40, 10x40, and 30x70 mm<sup>2</sup>. EBT3 film dosimetry results using the PDC were compared to the calibration curve actual dose for each film.

### 2.2.2.1 Water Phantom Spot-Check Measurements

The water phantom used for PDC verification consisted of a 3D-printed polylactic acid (PLA) film holder glued to the bottom of a plastic bowl, submerged in distilled water, and filled to 4 cm height from the bottom of the bowl. The PLA film holder is approximately 3 cm tall, with room to insert films at depths of 0, 2.5, 5, 10, and 20 mm. Through this setup, 10 mm of water would be beneath the deepest film. In this experiment, films were infixed to the slot at 10 mm depth (along the film holder), ensuring that 20 mm of water was above the film—simulating the nominal output reference conditions. A CBCT image was acquired and used to set the isocenter to the center of the film at 2 cm depth in water.

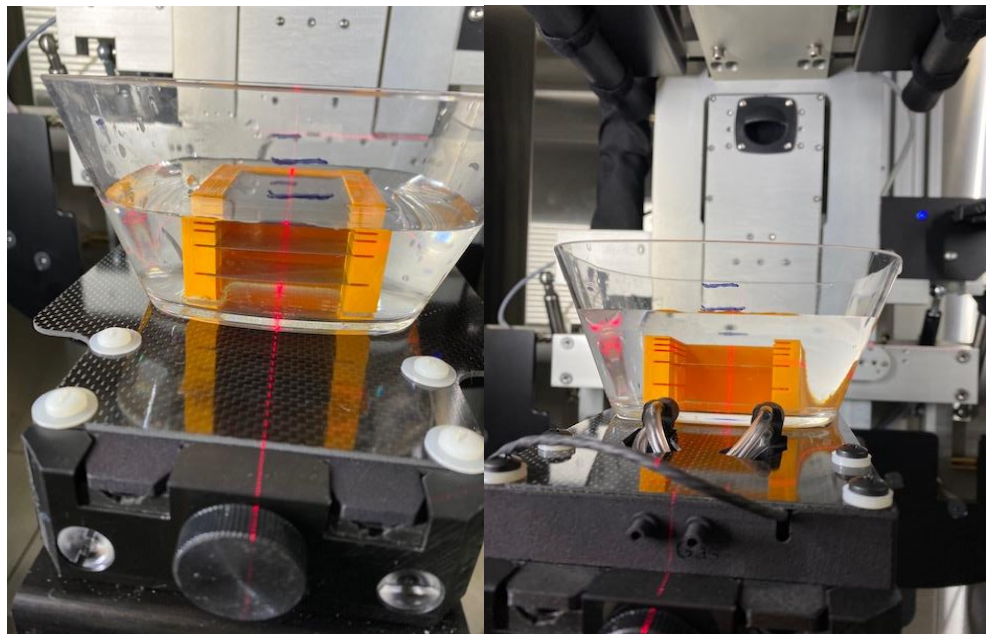


**Figure 13: Water phantom used for PDC verification (lasers set to isocenter).**

### **2.2.2.2 Bolus Phantom Spot-Check Measurements**

Bolus is a water-equivalent, solid material used commonly in radiotherapy to help treat superficial tumors found near the skin [23]. The added thickness of a tissue-equivalent material serves to circumvent tissue-sparing effects which may make it difficult to treat the aforementioned tumors. These characteristics, as well as its convenience for 2D dosimetry, made bolus a useful medium for EBT3 film dosimetry, and by extension, verification of the PDC.

To simulate reference conditions (2 cm), a 4 cm stack of 1 cm-thick bolus slabs was used. Similar to with the water phantom experiments, calibration curves were created by irradiating different films with 1 Gy, 2 Gy, 3 Gy, 4 Gy, 4.5 Gy, and 5 Gy, with each film being placed at 2 cm depth in the bolus stack. CBCT image was utilized to set the isocenter at the center of the film at 2 cm depth.

For verification of the PDC using the bolus phantom, a 2 cm stack was used. This methodology was used to vary the depth from reference conditions, considering that the water phantom PDC verification measurements were completed using the same setup as its associated calibration curve construction. Using this setup, each film was placed at 1 cm depth; the PDC was used to calculate an exposure time sufficient to deliver 4 Gy to 1 cm depth over the previously mentioned range of MVC field sizes.



**Figure 14: 2 cm Bolus phantom used for PDC verification (lasers set to isocenter).**

### **2.2.2.3 Mouse Phantom Spot-Check Measurements**

A tissue-equivalent mouse phantom was used to house the MOSFET detectors for the purpose of verifying the accuracy of the PDC with changing MVC field sizes. Using a mouse phantom, as opposed to the simple water and bolus phantoms, provided an opportunity to verify dose delivery with a more conventional mouse treatment setup using the PDC.

Two measurements using the MOSFET detectors were taken per MVC field size, with exposure time calculated using the PDC assuming 1 cm depth. Laser alignment was used to set the isocenter at the position of the MOSFET detector. Due to the lifespan of the MOSFET detectors, two different MOSFET detectors were used, being replaced after ten irradiations—each delivering approximately 4 Gy to the position of the MOSFET detector. SARRP treatment settings were 220 kVp and 13

mA. A farmer chamber was used for calibration of the MOSFET detectors, with the calibration factors for MOSFET detector 1 and 2 being 2.73 mV/cGy and 3.11 mV/cGy, respectively.



Figure 15: Calibration setup for MOSFET detectors using farmer chamber (left). PDC verification setup using MOSFET detectors inserted into mouse phantom as 1 cm depth (right).

### **2.3 Reproducing kV Mini-GRID Evaluation Methods using the XRAD 225Cx Small Animal Irradiator with the SARRP**

In terms of necessary experimental setup for GRID characterizations, the differences between the SARRP and the XRAD 225Cx are not particularly significant. As in Johnson *et al.*, mini-GRID evaluation methods were setup with a single AP beam at 225 kVp and 13 mA with the SARRP, delivering the equivalent of 6 Gy (exposure time calculated assuming open field, using the PDC) to EBT3 films infixed to a PLA film holder submerged in distilled water [18].

### **2.3.1 GRID Mount**

Two options for mounting the GRIDs were explored in Johnson *et al.*: collimator mount (otherwise denoted as “block tray” mount), and table mount. The block tray mount involved a more standard setup, with the GRIDs glued to a block tray, inserted into a 3D-printed PLA mount, and attached to the collimator approximately 6 cm from the film. The table setup brought the GRIDs considerably closer, being 3 cm from the film, and not attached to the collimator.

The results of Johnson *et al.* concluded that the table setup for mounting the GRIDs halved the penumbral region and increased the valley width of the GRID dose distribution by approximately 10% relative to the block tray setup (consequently increasing the sparing of lymphocytes) [18]. This benefit suggests that the results of characterizations using the table setup would have more practical implications for preclinical mouse trials. As such, it was decided the table mount would be used over the block tray mount.

#### **2.3.1.1 Table Mount**

A 3D-printed, 3 cm tall table was used for mounting the GRID. Each GRID used for characterizations was positioned on top of the mount. With the film being slotted in on the top level of the PLA film holder, the GRID was positioned exactly 3 cm above the film in each trial.

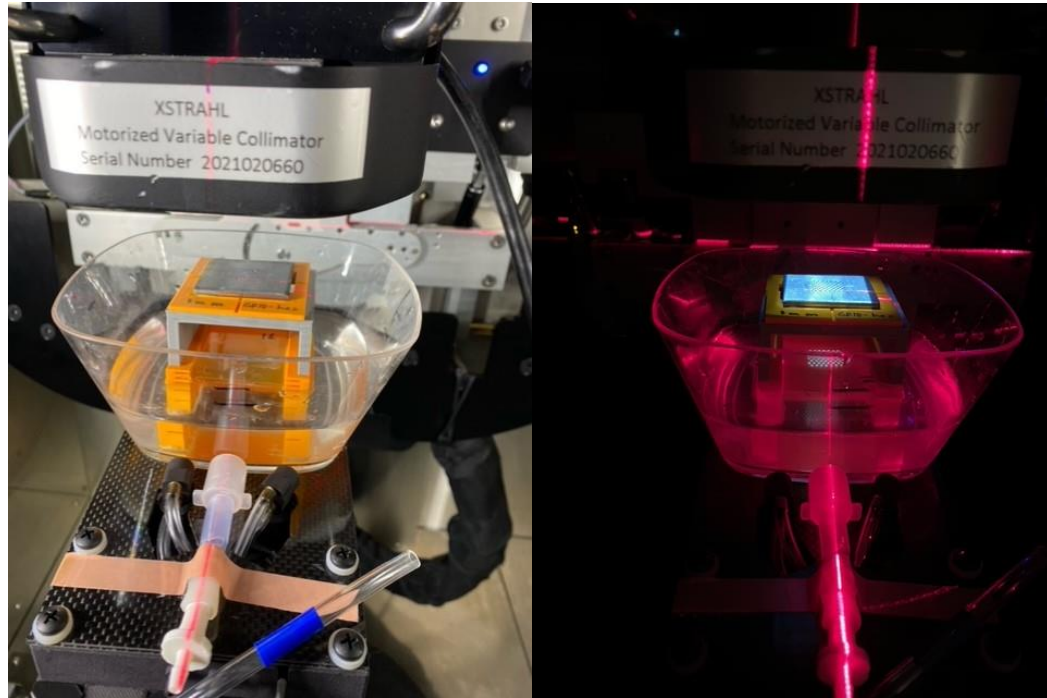


**Figure 16: Table mount setup used for GRID characterizations (left). SARRP cabinet lights turned off to accentuate laser alignment at isocenter (right).**

## **2.4 GRID Manufacturing and Design**

The GRIDs were designed by Tim Johnson, a former graduate student at Duke University and the lead author in Johnson *et al.* He utilized a 3D modeling software—Fusion 360—to configure and blueprint the GRIDs. These blueprints were subsequently sent to Duke University’s Physics Instrument shop to be machined [18].

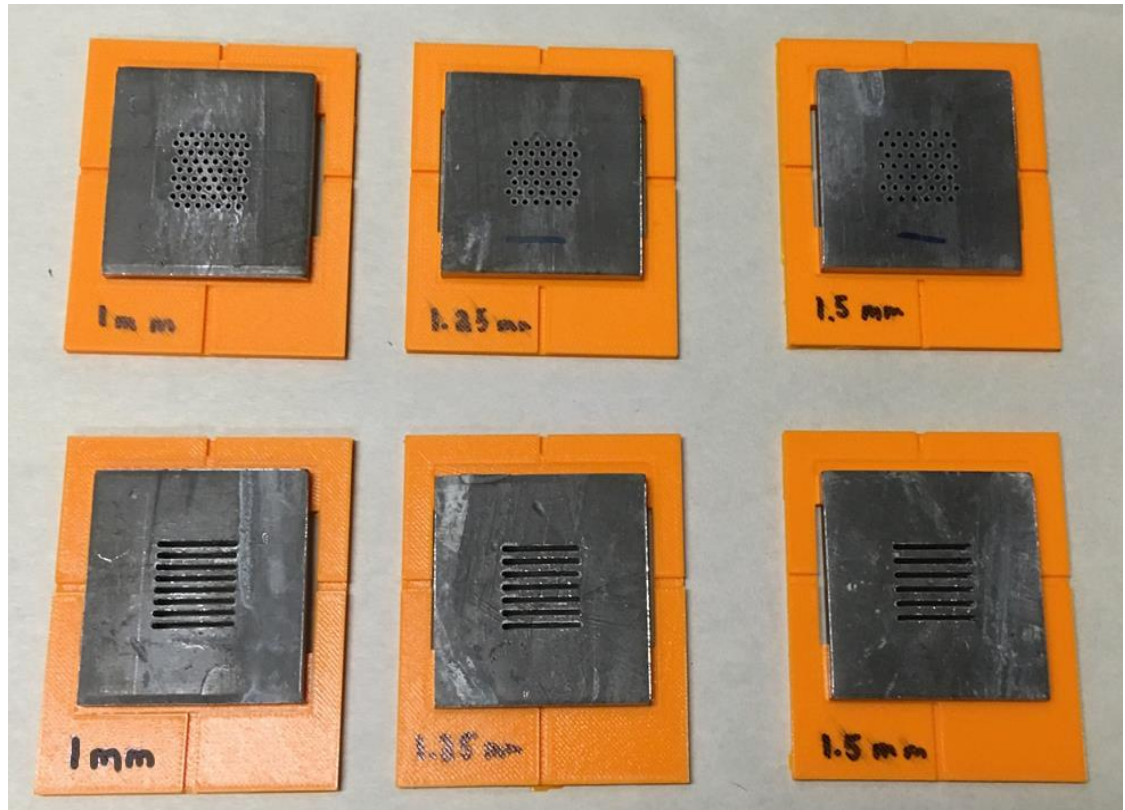


**Figure 17: Six mini-GRIDs—including three pencil GRIDs and three bar GRIDs—precision-milled from a 3 mm thick sheet of lead. Beamlet spacings are denoted in lower left corner of each GRID block tray [18].**

### **2.4.1 Material**

The GRIDs were manufactured out of a 3 mm lead sheet. They were designed dimensionally for use with the XRAD 225Cx small animal irradiator. Despite the XRAD 225Cx beam energy being 225 kVp, the average energy of the beam is approximately 75 kVp. As such, the specific thickness of lead chosen is sufficient to reduce the intensity of the incident beam to less than .005% intensity [18]. The beam energy for the SARRP is equivalent to that of the XRAD 225Cx, suggesting the current GRID thickness and material would be effective at attenuating the beam in the blocked areas of the GRIDs for the experiments of this thesis, as well as for future GRID therapy research at Duke University.

## 2.4.2 Beamlet Pattern and Spacing

Two different types of mini-GRIDs were used for the purposes of characterizations: pencil GRIDs and bar GRIDs. These designs each carry their own benefits and detriments, as well as their own characteristic arrangement of beamlets and beamlet spacing. Collectively, six GRIDs were manufactured for characterization purposes in Johnson *et al.*, including three pencil GRIDs and three bar GRIDs. Each pencil and bar GRID had different beamlet spacings (1 mm, 1.25 mm, 1.50 mm), with increasing beamlet spacing being found to correspond with higher output factors and peak-to-valley ratios [18]. The tradeoff of higher output factors and peak-to-valley ratios, however, was that a smaller percentage of the treatment volume received the prescription dose.

For this experiment, the goal was to explore the reproducibility of the results found in Johnson *et al.* using the Xstrahl SARRP, as opposed to the XRAD 225Cx. In pursuit of this goal, four GRIDs with varying beamlet patterns (two pencil GRIDs and two bar GRIDs) were selected for characterization.

### 2.4.2.1 Pencil GRID

The pencil GRIDs used for characterizations had 1 mm and 1.25 mm beamlet spacing, as well as consisting of 3 mm of lead thickness for the purpose of attenuation. It was determined in Johnson *et al.* that a hexagonal array of beamlets was advantageous to a square arrangement, as in a hexagonal arrangement, each beamlet is equidistant from one another [18]. Consequently, the valley dose between each beamlet will be identical across the treatment volume. Pencil GRIDs were also

determined to have higher output factors and peak-to-valley ratios than the bar GRIDs in Johnson *et al.* for the same beamlet spacing.

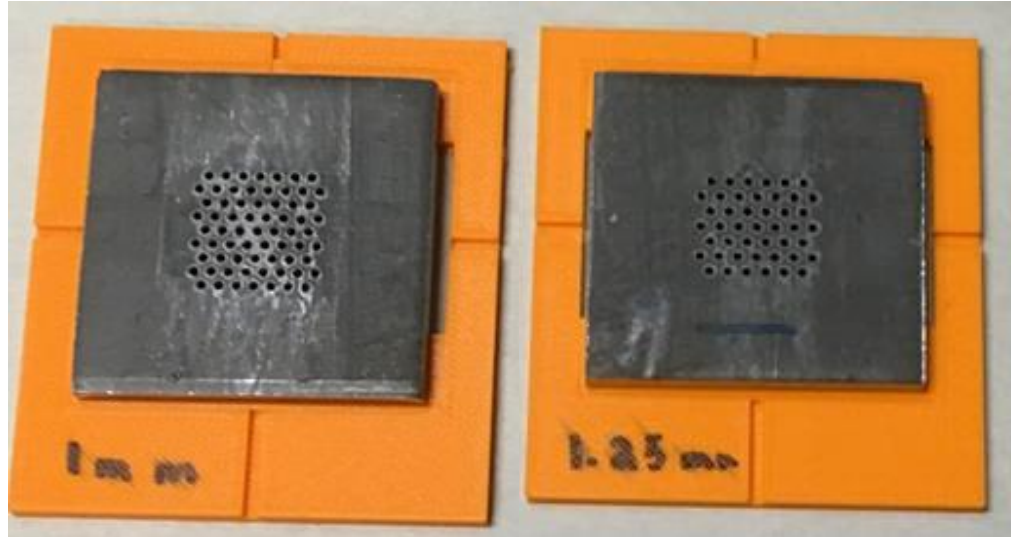


**Figure 18: 1 mm (left) and 1.25 mm (right) beamlet spacing pencil GRIDs used for GRID characterizations.**

#### **2.4.2.2 Bar GRID**

The bar GRIDs used for characterizations had 1.00 mm and 1.25 mm beamlet spacing, in addition to the standardized 3 mm thickness of lead used for the other GRIDs manufactured at Duke University. As a contrast to pencil GRIDs, bar GRIDs have lower output factors and peak-to-valley ratios for equivalent beamlet spacings in pencil GRIDs; however, they are able to achieve much higher target coverage than pencil GRIDs, which ultimately require more holes with shorter beamlet spacing in order to achieve similar coverage [24].

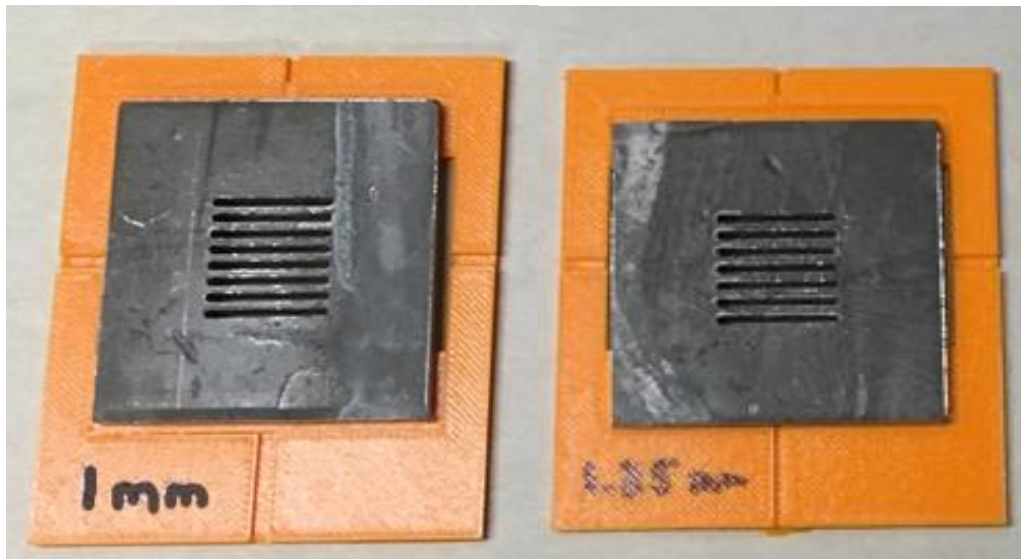
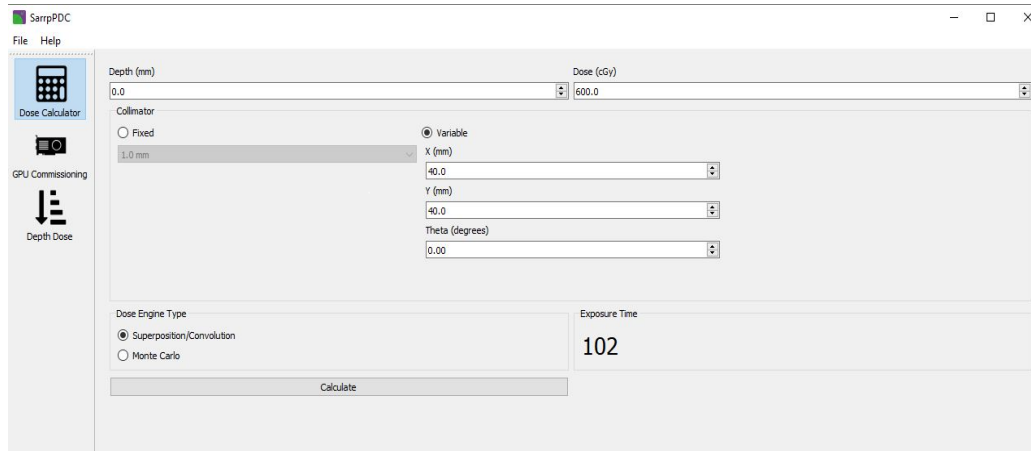


Figure 19: 1.00 mm (left) and 1.25 mm (right) beamlet spacing bar GRID used for GRID characterizations.

## 2.5 GRID Characterizations

GRID characterizations were performed using the aforementioned table mount setup shown in Figure 15. As discussed in section 2.3, irradiation settings and procedure were nearly identical to those used to verify the PDC, including 220 kVp, 13 mA, as well as the use of an acquired CBCT to position the isocenter at the center of the film at 0 cm depth in distilled water. A 40 mm x 40 mm MVC field size was used for the GRID characterizations, mimicking the treatment geometry established in Johnson *et al.*, which used a 40 mm x 40 mm treatment cone.

The PDC was used to prescribe 6 Gy to 0 cm depth using a 40 x 40 mm<sup>2</sup> MVC field size, yielding a necessary exposure time of 102 seconds. Films were infixed to the top slot of the PLA film holder, with room temperature distilled water being used to fill the water phantom bowl to the height of the film (3 cm)—such that the film is on the surface, as in Johnson *et al* [18].



**Figure 20: PDC exposure time calculation for GRID irradiations. User inputs include MVC field size (40x40 mm<sup>2</sup>), depth (0 cm), dose (600 cGy), and gantry angle (which for all experiments thus far has been 0). The superposition/convolution algorithm was used to calculate exposure time, which yielded 102 seconds to administer 6 Gy.**

### 2.5.1 Peak-to-Valley Ratio

GRIDs are often characterized in literature using a ratio of maximum peak dose to minimum adjacent valley dose; this ratio is denoted as the peak-to-valley ratio [16, 24]. In principle, a higher peak-to-valley ratio is more optimal than a lower peak-to-valley ratio, as improved tumor control in GRID therapy comes from the sparing of lymphocytes. Optimizing peak-to-valley ratio and percent area treated was a concept explored in Johnson *et al.*, making it important to ensure reproducibility in measuring this core GRID characteristic using the SARRP [18].

Peak-to-valley ratio was measured using ImageJ. Line profiles were drawn through the central axis of both the pencil GRIDs and bar GRIDs. Data was collected from these line profiles and imported into Microsoft Excel. Using an EBT3 calibration curve acquired on the day of measurement, optical density change values (relative to pre-scan values) from line profiles were converted to dose.

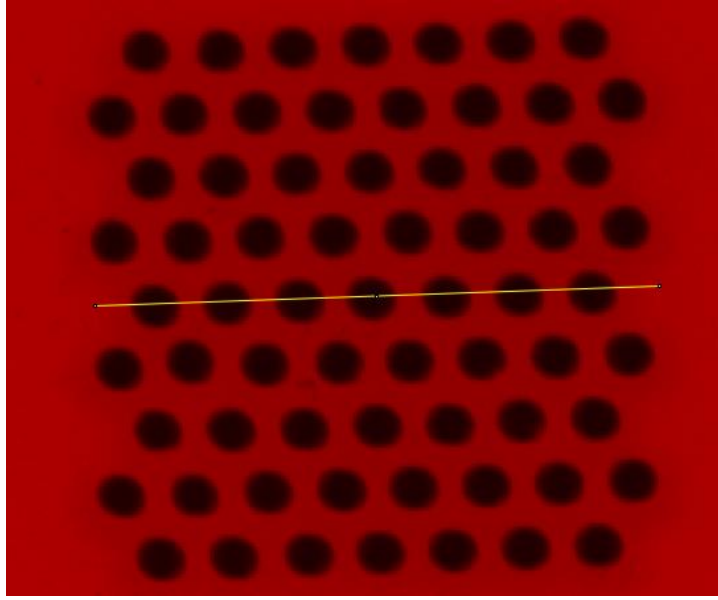


**Figure 21: Line profile drawn in ImageJ for evaluating peak-to-valley ratio of 1 mm beamlet spacing pencil GRID.**

Using the dose data acquired, the following equation was utilized to compute the peak-to-valley ratio for both the pencil and bar GRID:

$$Peak:Valley = \frac{Maximum\ Peak\ Dose}{Minimum\ Adjacent\ Valley\ Dose} \quad (Eq. 5)$$

### **2.5.2 Output Factor**

Output factors are used to scale the output of the Xstrahl SARRP when using a GRID for treatment. Output factors were defined using the equation listed below:

$$Output\ Factor = \frac{Average\ Peak\ Dose}{Delivered\ Dose\ with\ Open\ Field} \quad (Eq. 6)$$

ImageJ was used to acquire average peak pixel intensity values. Peak dose values for each individual beamlet were averaged by first using equation 4 to convert change in optical density values to dose from pre-scans and post-scans. An identical irradiation was performed using an open field (no GRID), delivering 6 Gy

to a film set at isocenter. Using equation 6, the averaged peak dose value was divided by the dose ascertained via this unblocked field measurement.

### **2.5.3 Dose Map**

Using an in-house MATLAB code developed by Timothy Johnson at Duke University, film scans were converted into maps of absolute dose [18]. These conversions were completed using the same calibration curve utilized for evaluating the peak-to-valley ratio and output factor for the pencil and bar GRIDs. Subsequently, these absolute dose maps were converted to relative dose maps; this was done by dividing the absolute dose across the image by the average peak dose of the GRIDs (same value as defined in Equation 6). The results of these acquired dose maps were compared to those produced in Johnson *et al.*

#### **2.5.3.1 Dose Volume Histogram**

A dose volume histogram (DVH) is defined as a plot of the dose-volume frequency distribution, illustrating the relative dose delivered with respect to percent volume treated [25]. The in-house MATLAB code used to acquire the relative dose maps for the GRIDs in Johnson *et al.* was also used to generate DVHs for both the pencil and bar GRIDs.

#### **2.5.3.2 Integral Dose Relative to Open Field**

Integral dose is a measurement used to quantify the cumulative dose delivered during treatment. For convenience, as well as consistency with core GRID measurements conducted in Johnson *et al.*, integral dose was instead measured as integral dose relative to open field. This measurement assumes that since the volume

of each film is identical to one another (thickness being assumed identical, and each film being roughly 4 cm x 4 cm), the integral dose can be compared to the integral dose delivered by an open field. This relationship is demonstrated below, and was calculated using the in-house MATLAB code discussed in Section 2.5.3 and Subsection 2.5.3.1:

$$\text{Integral Dose} = V_{film} * (D_{av})_{GRID} = (D_{av})_{GRID}$$

$$\text{Integral Dose} = V_{film} * (D_{av})_{Open\ field} = (D_{av})_{Open\ field}$$

$$\text{Integral Dose Relative to Open Field} = \frac{V_{film} * (D_{av})_{GRID}}{V_{film} * (D_{av})_{Open\ field}}$$

$$\text{Integral Dose Relative to Open Field} = \frac{(D_{av})_{GRID}}{(D_{av})_{Open\ field}} \quad (\text{Eq. 7})$$

### 3. Results

The percent difference equation used to measure the effective reproducibility of the experimental results is demonstrated in Equation 8:

$$\text{Percent Difference} = \frac{|V_1 - V_2|}{\left[\frac{V_1 + V_2}{2}\right]} * 100 \quad (\text{Eq. 8})$$

where  $V_1$  is the experimentally measured value, and  $V_2$  is the value for comparison—whether that value be from Johnson *et al.* or the Xstrahl factory commissioning results. This was used for all tables listing percent difference (except Table 17).

#### 3.1 Verifying Xstrahl Factory Commissioning Results

##### 3.1.1 TG-61 Output Measurement

**Table 6: TG-61 calculation table used for evaluating the Xstrahl SARRP TG-61 dose rate (or output). Measured output is the average of three individual measurements.**

Temperature (°C)	Pressure (inHg)	Temperature-Pressure Correction Factor ( $P_{TP}$ )	Beam Energy (kVp)	Beam Current (mA)	Exposure Time (seconds)	Constancy Reading	TG-61 Measured Output (Gy/min)
20.0	29.9	6.95	220	13	60	7	3.66

TG-61 output was experimentally measured to be 3.66 Gy/min, as indicated in Table 6. Measured temperature and pressure on the day of measurement are listed in column 1 and column 2 of Table 6, with the correction factor for temperature and pressure (Equation 2) used for calculation of TG-61 output listed in column 3.

**Table 7: Comparison of experimentally measured TG-61 output to manufacturer measured TG-61 output. Percent difference between these values was calculated using Equation 8.**

Experimentally Measured TG-61 Output (Gy/min)	Manufacturer Measured TG-61 Output (Gy/min)	Percent Difference (%)
3.66	3.66	0

The percent difference between the experimentally measured TG-61 output and the manufacturer measured TG-61 output was determined to be approximately 0%. This indicates that there was no difference between the experimentally measured value and the expected measured value for the TG-61 output.

### 3.1.2 Half-Value Layer

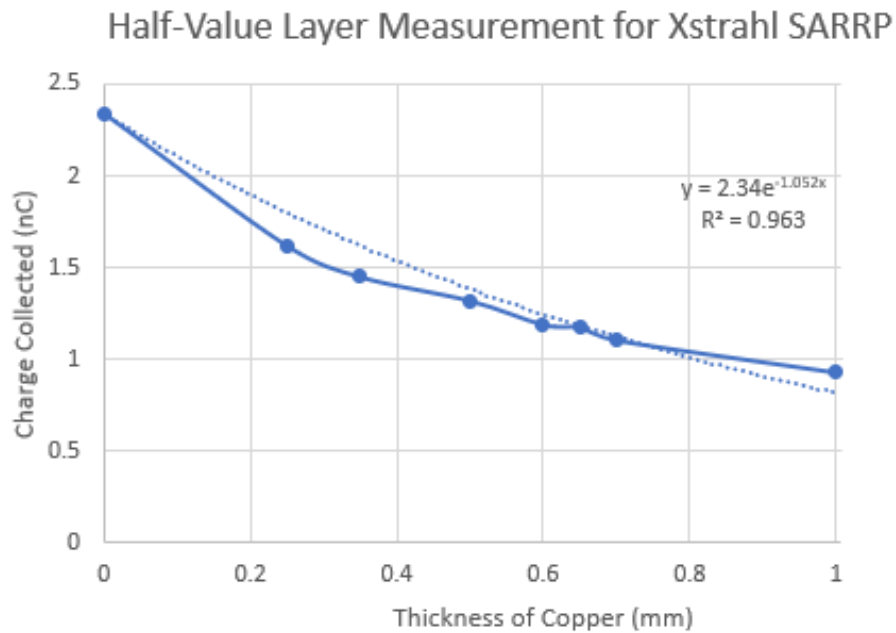


**Figure 22: Plot illustrating measured charge collected values with respect to increasing thickness of copper. Data was fitted to an exponential decay curve with standard exponential decay curve being depicted as a dotted blue line adjacent to the experimentally plotted solid blue line.**

The results of the HVL measurement were plotted in Microsoft Excel, as illustrated by Figure 22. Using the exponential decay equation derived by fitting the acquired HVL data to an exponential decay curve, the HVL was determined to be .66 mm of copper. This value was compared to the Xstrahl measured HVL (.67 mm of copper) in Table 8.

**Table 8: Comparison of experimentally measured HVL to manufacturer HVL using copper. Percent difference between these values was calculated using Equation 8.**

<b>Experimentally Measured HVL (mm Cu)</b>	<b>Manufacturer Measured HVL (mm Cu)</b>	<b>Percent Difference (%)</b>
.66	.67	1.5

The measured percent difference between the experimentally measured HVL and the manufacturer measured HVL was approximately 1.5%. This value demonstrates a minor difference between the HVL measured at Duke University, and the HVL measured during the commissioning process for the SARRP.

### ***3.2 Verifying the Accuracy of the MuriPlan Integrated Point Dose Calculator***

#### **3.2.1 Water Phantom Spot-Check Measurements**

Prior to performing the necessary irradiations for validating the PDC, calibration curve data points (open blue circles) were fitted to a 3rd degree polynomial (dotted blue line), as demonstrated in Figure 23:

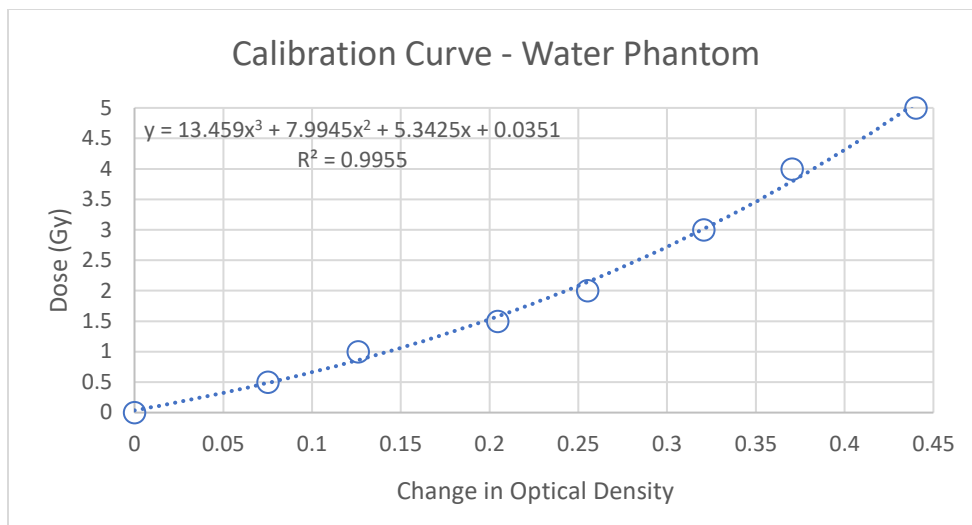


**Figure 23: EBT3 film calibration curve generated for water phantom on November 9<sup>th</sup>, 2021. Data was fitted to 3<sup>rd</sup> degree polynomial equation, listed in the upper left corner of the plot, along with the computed R<sup>2</sup> value to evaluate the fit of the data to the polynomial curve.**

Water phantom verification measurements for the PDC involved testing six different MVC field sizes across two different depths (0 cm, 2 cm).

**Table 9: Water phantom measurements acquired for verification of the PDC. Exposure time was calculated using the PDC. PDC inputted dose was 300 cGy across all trials, except for 400 cGy when testing the 35 mm x 35 mm MVC field. Two measurements were taken per field size, with pixel intensities averaged prior to use of calibration curve equation to calculate film measured dose. Percent difference is calculated in column 5, with red text indicating potentially invalid or concerning measurements.**

Technique	Exposure Time (seconds)	PDC Dose (cGy)	Film Measured, using calibration curve (cGy)	Percent Difference (%)
Field = 10x10 Depth = 2cm	88	300	279.4	-6.86
Field = 20x20 Depth = 2cm	78	300	390.9	23.3
Field = 30x30 Depth = 2cm	69	300	270.2	-9.93
Field = 10x40 Depth = 2cm	76	300	342.4	14.1
Field = 10x20 Depth = 2cm	81	300	268.3	-10.6
Field = 35x35 Depth = 0cm	69	400	379.4	5.15

Due to the intrinsic volatility of EBT3 film measurements at low energy levels (75 kVp average energy for the SARRP beam), percent differences in the range of 0% to 10% were considered to be in good agreement with the PDC-predicted dose. Four out of the six tested field sizes were evaluated to be in good agreement with the PDC-predicted dose. Relatively high percent errors were noted with the 20 mm x 20 mm field and 10 mm x 40 mm MVC field sizes.

### 3.2.2 Bolus Phantom Spot-Check Measurements

Like with the water phantom, prior to evaluating the PDC accuracy, a separate EBT3 film calibration curve was created for the bolus phantom, with calibration curve data points (open blue circles) being fitted to a 3rd degree polynomial (dotted blue line), as demonstrated in Figure 24:

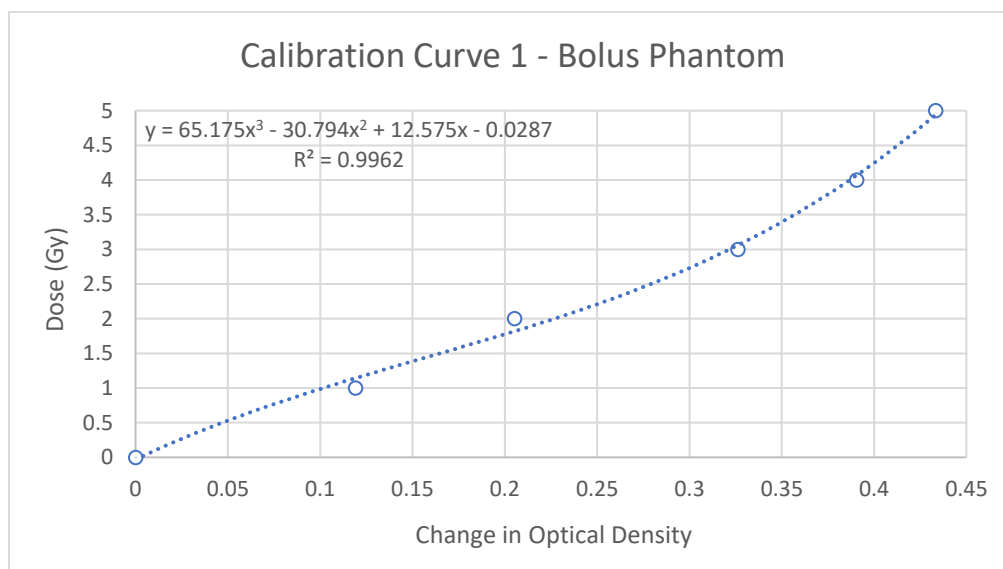


**Figure 24: EBT3 film calibration curve generated for bolus phantom on November 16<sup>th</sup>, 2021. Data was fitted to 3<sup>rd</sup> degree polynomial equation, listed in the upper left corner of the plot, along with the computed R<sup>2</sup> value to evaluate the fit of the data to the polynomial curve.**

Bolus phantom verification measurements on November 16th, 2021, tested six different MVC field sizes all at 1 cm depth. The results of these measurements are displayed in Table 10:

**Table 10: First bolus phantom measurements acquired for verification of the PDC (November 16<sup>th</sup>). Exposure time was calculated using the PDC. PDC inputted dose was 400 cGy across all trials. Two measurements were taken per field size, with pixel intensities averaged prior to use of calibration curve equation to calculate film measured dose. Percent difference is calculated in column 5, with red text indicating potentially invalid or concerning measurements. The 20 mm x 10 mm field size was not tested on this measurement day.**

Technique	Exposure Time (seconds)	PDC Dose (cGy)	Film Measured, using calibration curve (cGy)	Percent Difference (%)
Field = 10x10 Depth = 1cm	92	400	420.1	4.88
Field = 10x20 Depth = 1cm	87	400	310.2	-25.35
Field = 20x10 Depth = 1cm	88	400	N/A	N/A
Field = 10x40 Depth = 1cm	84	400	310.1	-25.35
Field = 20x20 Depth = 1cm	84	400	393.7	-1.77
Field = 30x30 Depth = 1cm	77	400	382.4	-4.60
Field = 40x40 Depth = 1cm	73	400	382.0	-4.60

Four of the six MVC field sizes tested using the PDC on November 16th, 2021, demonstrated good agreement between the film measured dose and the PDC-predicted dose. The 10 mm x 20 mm and 10 x 40 mm MVC field size film measurements did not demonstrate good agreement with the PDC-predicted dose, with an approximately 25% error being present in both trials.

Additional bolus phantom measurements were collected on November 24<sup>th</sup>, 2021, prompting the creation of a secondary calibration curve to ensure consistency with the data collected on November 16<sup>th</sup>. This second calibration curve is displayed in Figure 25:

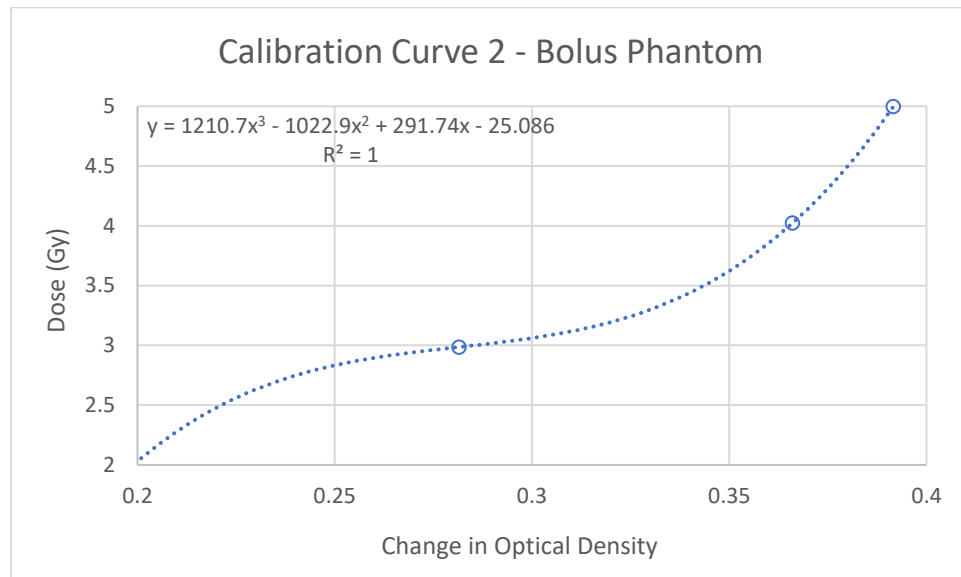


**Figure 25: EBT3 film calibration curve generated for bolus phantom on November 24<sup>th</sup>, 2021. Data was fitted to 3<sup>rd</sup> degree polynomial equation, listed in the upper left corner of the plot, along with the computed R<sup>2</sup> value to evaluate the fit of the data to the polynomial curve. Measured doses for this calibration curve included 2 Gy, 3 Gy, 4 Gy, and 5 Gy, with the aim of improving measurement accuracy since the PDC-predicted dose was 4 Gy.**

The calibration curve in Figure 25 was utilized to determine the film measured dose for experiments conducted on November 24<sup>th</sup>, which tested seven different MVC field sizes all at 1 cm depth.

**Table 11: Second bolus phantom measurements acquired for verification of the PDC (November 24<sup>th</sup>). Exposure time was calculated using the PDC. PDC inputted dose was 400 cGy across all trials. Two measurements were taken per field size, with pixel intensities averaged prior to use of calibration curve equation to calculate film measured dose. Percent difference is calculated in column 5, with red text indicating potentially invalid or concerning measurements.**

Technique	Exposure Time (seconds)	PDC Dose (cGy)	Film Measured, using calibration curve (cGy)	Percent Difference (%)
Field = 10x10 Depth = 1cm	92	400	399.3	-0.20
Field = 10x20 Depth = 1cm	87	400	316.1	-23.4
Field = 20x10 Depth = 1cm	88	400	408.8	2.18
Field = 15x40 Depth = 1cm	81	400	314.5	-23.95
Field = 20x20 Depth = 1cm	84	400	402.0	0.50
Field = 30x30 Depth = 1cm	77	400	311.6	-24.83
Field = 40x40 Depth = 1cm	73	400	311.2	-25.00

Significantly more disagreement was noted in the results of the November 24<sup>th</sup> bolus phantom measurements, with only three of the seven MVC field sizes tested being in good agreement with the PDC-predicted dose. The four fields that were not in good agreement—the 10 mm x 20 mm, 15 mm x 40 mm, 30 mm x 30 mm, and 40 mm x 40 mm—demonstrated percent differences of larger than 20% in each case. By contrast, the percent difference associated with the three other fields—the 10 mm x 10 mm, 20 mm x 10 mm, and 20 mm x 20 mm—demonstrated exceptional

agreement with the PDC-predicated dose, with percent differences as low as 0.20% and as high as 2.18%.

### 3.2.3 Mouse Phantom Spot-Check Measurements

**Table 12: Mouse phantom measurements acquired for verification of the PDC (January 7<sup>th</sup>). Exposure time was calculated using the PDC. PDC inputted dose was 400 cGy across all trials. MOSFET measured dose is indicated in column 4. Percent difference is calculated in column 5, with red text indicating potentially invalid or concerning measurements.**

**\* Measurement is an outlier, as the sensitive volume for the detector was slightly out of field.**

Technique	Exposure Time (seconds)	PDC Dose (cGy)	MOSFET Measured (cGy)	Percent Difference (%)
Field = 30x70 Depth = 1cm	72	400	376.8	-5.97
Field = 10x10 Depth = 1cm	90	400	421.8	5.31
Field = 20x20 Depth = 1cm	83	400	415.8	2.18
Field = 30x30 Depth = 1cm	76	400	388.2	-2.99
Field = 40x40 Depth = 1cm	73	400	379.0	-5.39
Field = 10x20 Depth = 1cm	86	400	332.8*	-18.3*
Field = 10x40 Depth = 1cm	82	400	400.5	.120
Field = 20x10 Depth = 1cm	86	400	403.7	.920

Table 12 depicts the results of the mouse phantom spot-check measurements for verification of the PDC, conducted using MOSFET detectors, instead of EBT3 film, to measure dose. Eight different MVC field sizes were measured, all at 1 cm depth. Good agreement with the PDC-predicted dose using the MOSFET detectors was determined to be approximately 6% or below, due to the superior ability of

MOSFET detectors for small field dosimetry at low photon beam energies relative to EBT3 film.

The results of these measurements were that seven of the eight MVC field sizes tested demonstrated good agreement with the PDC-predicted dose. The single field that did not demonstrate good agreement with the PDC-predicted dose was the 10 mm x 20 mm MVC field size, which had a percent difference of approximately 18.3%. This was assessed to likely be a measurement error, as prior to the 10 mm x 20 mm measurement, the MOSFET detector needed to be replaced, as it had reached its dose threshold. In replacing the detector, it is highly plausible that only a portion of the sensitive volume occupied the 10 mm x 20 mm field, limiting the amount of dose absorbed by the MOSFET detector.

### **3.2.4 MuriPlan Simulations**

Table 13 displays the results of the MuriPlan treatment planning simulations for the bolus phantom treatment adjacent to the film measured dose for the same field size and depth. It also displays the percent difference between the MuriPlan simulated dose and the film-measured dose.

**Table 13: Comparison of bolus phantom PDC-predicted dose, MuriPlan simulation results, and film measured dose on November 16th.**

**\*: Film measured dose value for 20x10 field was acquired on different measurement day (November 24<sup>th</sup>) and used bolus calibration curve 2.**

<b>Technique</b>	<b>PDC Dose (cGy)</b>	<b>Film measured dose using bolus calibration curve 1 (cGy)</b>	<b>MuriPlan simulation predicted dose (cGy)</b>	<b>Percent Difference between PDC dose and simulation (%)</b>	<b>Percent Difference between film dosimetry and simulation (%)</b>
Field = 10x10 Depth = 1cm	400	420.1	371.0	-7.52	-12.4
Field = 10x20 Depth = 1cm	400	310.2	366.0	-8.87	-16.5
Field = 20x10 Depth = 1cm	400	408.8*	369.3	-7.98	-10.1
Field = 10x40 Depth = 1cm	400	310.1	386.9	-3.33	-22.0
Field = 20x20 Depth = 1cm	400	393.7	374.1	-6.69	-5.11
Field = 30x30 Depth = 1cm	400	382.4	374.5	-6.58	-2.09
Field = 40x40 Depth = 1cm	400	382.0	371.3	-7.44	-2.84

Percent differences between the EBT3 film dose measurements and the MuriPlan simulations for the same bolus phantom range from a low of 2.09% to a high for 22.0%. Increased difference was seen in the films which deviated most from

the PDC-predicted dose for the bolus phantom, including the 10 mm x 20 mm (16.5%) and 10 mm x 40 mm measurements (22.0%).

**Table 14: Comparison of water phantom PDC-predicted dose, MuriPlan simulation results, and film measured dose on November 9th.**

<b>Technique</b>	<b>PDC Dose (cGy)</b>	<b>Film measured dose using water calibration curve (cGy)</b>	<b>MuriPlan simulation predicted dose (cGy)</b>	<b>Percent Difference between PDC dose and MuriPlan simulation (%)</b>	<b>Percent Difference between film dosimetry and MuriPlan simulation (%)</b>
Field = 10x10 Depth = 2cm	300	279.4	288.9	-3.76	-3.34
Field = 10x20 Depth = 2cm	300	342.4	298.5	-.501	13.7
Field = 10x40 Depth = 2cm	300	268.3	294.2	-1.95	-9.2
Field = 20x20 Depth = 2cm	300	390.9	297.7	-.769	27.1
Field = 30x30 Depth = 2cm	300	270.2	302.5	.830	-11.3

Stronger agreement was observed between the PDC-predicted dose and the MuriPlan simulation predicted dose for the water phantom relative to the bolus phantom. The PDC assumes water equivalence; the water phantom was segmented as an entirely homogeneous water phantom in MuriPlan, whereas the bolus phantom was segmented in MuriPlan as being tissue equivalent. Consequently, it

was predicted that these two dose calculation mechanisms would have better agreement for the water phantom than the bolus phantom, which is represented by the data in Table 14.

Percent difference between the film dosimetry and MuriPlan simulation results for the water phantom showed reasonable agreement, with percent differences ranging from 3% to 14% for 4/5 measured MVC field sizes, with a single outlier being the 20x20 mm<sup>2</sup> film measurement (which was subsequently identified to be anomalous using the MOSFET detector to verify the result).

Compared to the film measurements, there was considerably more agreement between the MuriPlan simulation-predicted dose and the PDC-predicted dose. EBT3 film measurements had fairly inconsistent agreement with the PDC-predicted dose due to the characteristic uncertainty of EBT3 film; by contrast, the MuriPlan simulations retained a fairly consistent percent difference of approximately .5% to 8% from the PDC-predicted dose.

### 3.3 GRID Characterizations

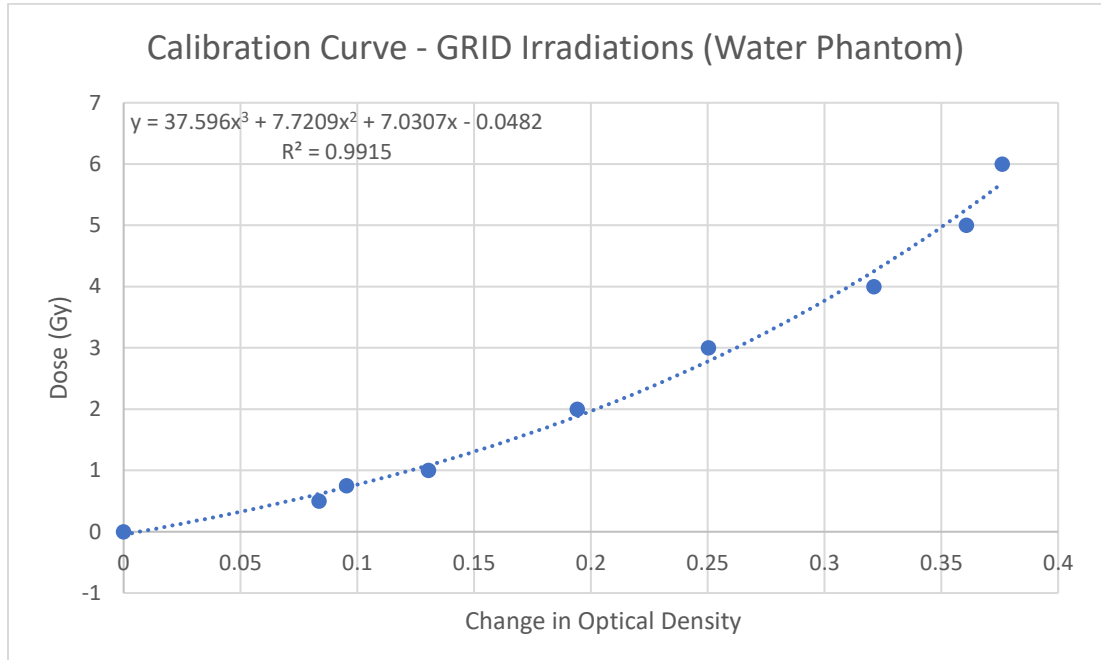


**Figure 26: Calibration curve created using water phantom for GRID irradiations on April 11th, 2022.**

The calibration curve illustrated above in Figure 26 was utilized for EBT3 film dosimetry in the GRID characterization stage of this experiment. The water phantom setup used for this calibration curve was nearly identical to the water phantom setup used for verification of the PDC, with the exception of water being filled to the top film slot of the PLA film holder, and the PDC being used to determine the exposure time for each calibration curve data point. Notably, across calibration curves, there was considerable uncertainty in estimating dose in the valley regions of the GRID due to limitations of EBT3 film sensitivity below .2 Gy.

#### 3.3.1 Peak-to-Valley Ratio

The peak-to-valley ratios calculated using EBT3 film results acquired on April 11th, 2022, are displayed in Table 15 below:

**Table 15: Comparison of experimental peak:valley ratios measured for the 20x20 mm<sup>2</sup> pencil and bar GRIDs (1 mm and 1.25 mm beamlet spacing, measured on April 11th, 2022, using the SARRP) with peak:valley ratios measured for the same GRIDs using the XRAD 225Cx in Johnson *et al* [18].**

<b>Grid Type</b>	<b>Peak:Valley Ratio (SARRP)</b>	<b>Peak:Valley Ratio (XRAD 225Cx)</b>	<b>Percent Difference (%)</b>
Pencil GRID, 1 mm beamlet spacing	24.5 ± 0.6	18.7 ± 0.6	26.8
Pencil GRID, 1.25 mm beamlet spacing	25.1 ± 1.3	26.3 ± 1.5	4.67
Bar GRID, 1 mm beamlet spacing	13.2 ± 1.1	11.9 ± 0.9	10.4
Bar GRID, 1.25 mm beamlet spacing	18.5 ± 1.2	13.6 ± 0.4	30.5

Between 4.67% and 30.5% difference was observed between experimental measurements of peak:valley ratio and the results demonstrated in Johnson *et al*. Despite varying degrees of percent difference, the expected relationship between beamlet pattern/spacing and peak:valley ratio was able to be reproduced in this experiment using the SARRP. Higher peak:valley ratios for equivalent beamlet spacing were measured for pencil GRIDs relative to bar GRIDs (24.5 ± 0.6 and 25.1 ± 1.3 to 13.2 ± 1.1 and 18.5 ± 1.2, respectively), with increasing beamlet spacing being consistent with higher peak:valley ratios for both GRID types.

Higher peak:valley ratios were measured for the pencil GRIDs in this experiment compared to those measured for the same GRIDs in Johnson *et al*. Similarly, higher peak:valley ratios were found for the characterized bar GRIDs compared to those measured in Johnson *et al.*, as well.

### 3.3.2 Output Factor

The output factors calculated using the EBT3 film results acquired on April 11th, 2022, are displayed in Table 16:

**Table 16: Comparison of experimental output factors measured for the 20x20 mm<sup>2</sup> pencil and bar GRIDs (1 mm and 1.25 mm beamlet spacing, measured on April 11th, 2022, using the SARRP) with output factors measured for the same GRIDs using the XRAD 225Cx in Johnson *et al* [18]. Red text indicates potentially invalid or concerning measurements.**

Grid Type	Output Factor (SARRP)	Output Factor (XRAD 225Cx)	Percent Difference (%)
Pencil GRID, 1 mm beamlet spacing	.77 ± .03	.76 ± .01	1.00
Pencil GRID, 1.25 mm beamlet spacing	.74 ± .02	.74 ± .01	0.00
Bar GRID, 1 mm beamlet spacing	.83 ± .03	.69 ± .01	14.00
Bar GRID, 1.25 mm beamlet spacing	.80 ± .03	.68 ± .01	12.00

In large part, experimentally measured output factors corroborated the results demonstrated in Johnson *et al.*, with percent differences ranging from a low of 0%, to a high of 14%. Particularly exceptional agreement was observed in the output factor measurements for the pencil GRIDs, with the 1 mm and 1.25 mm beamlet spacing GRIDs measured using the SARRP having a 1% and 0% difference, respectively, from those measured using the XRAD 225Cx in Johnson *et al.* Higher output factors were measured for both bar GRIDs in this experiment relative to those using the XRAD 225Cx (.83 ± .03 and .80 ± .03 compared to .69 ± .01 and .68 ± .01 in Johnson *et al.*). Both bar GRID output factors were higher than those measured for the pencil GRIDs with equivalent beamlet spacing—a trend which was not observed in Johnson *et al.*

### 3.3.3 Dose Map

Figure 27 and Figure 28 display a side-by-side comparison of relative dose maps for the  $20 \times 20 \text{ mm}^2$  pencil and bar GRIDs, respectively, evaluated in this experiment versus those generated in Johnson *et al.*:

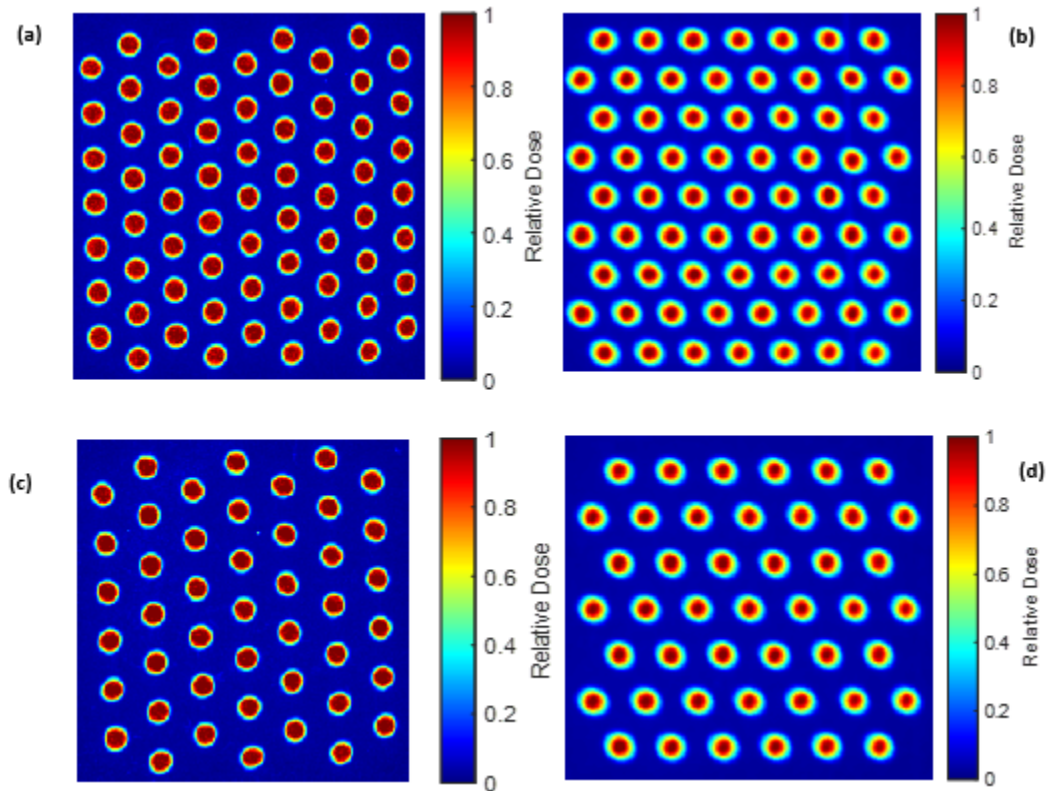
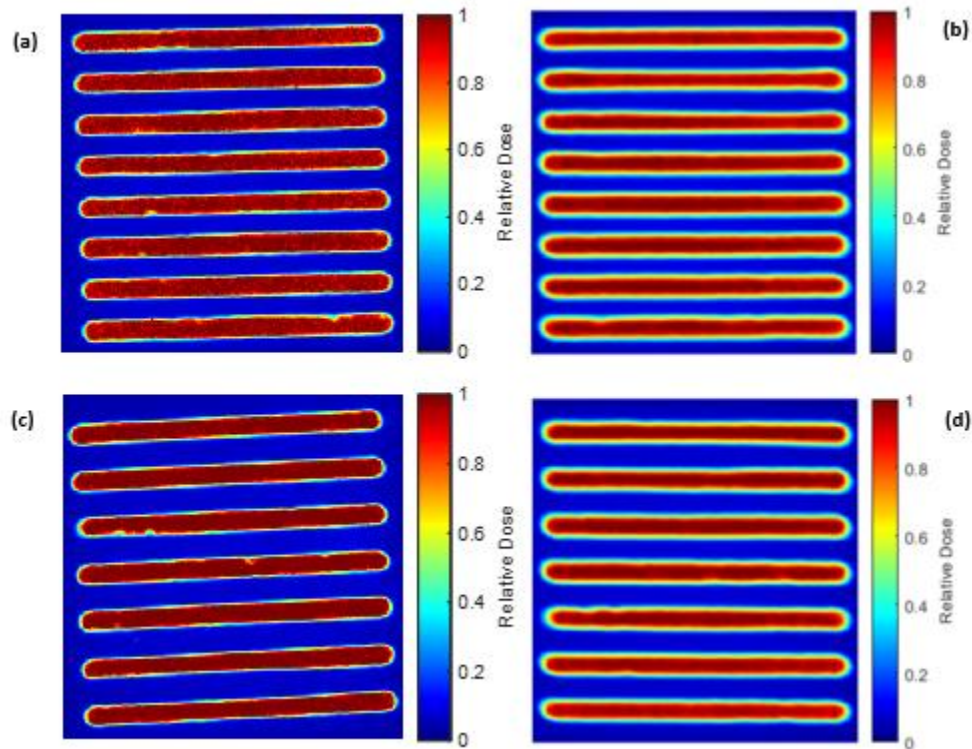


Figure 27: (a) Relative dose map for  $20 \times 20 \text{ mm}^2$  pencil GRID with 1 mm beamlet spacing (this experiment). (b) Relative dose map for  $20 \times 20 \text{ mm}^2$  pencil GRID with 1 mm beamlet spacing (Johnson *et al.*) [18]. (c) Relative dose map for  $20 \times 20 \text{ mm}^2$  pencil GRID with 1.25 mm beamlet spacing (this experiment). (d) Relative dose map for  $20 \times 20 \text{ mm}^2$  pencil GRID with 1.25 mm beamlet spacing (Johnson *et al.*).

Initial analysis of the relative dose maps for the characterized pencil GRIDs demonstrates acceptable agreement with those produced for Johnson *et al.* However, more high dose uniformity (rather, dose above 80% of the average peak dose) was observed in the beamlets for the evaluated pencil GRIDs relative to those in Johnson

*et al.* Additionally, the dose maps in Figure 27 suggest that there were lower valley doses in between the individual beamlets, implying that more valley lymphocytes would be spared using the SARRP than the XRAD 225Cx – assuming the same GRIDs.



**Figure 28: (a) Relative dose map for 20x20 mm<sup>2</sup> bar GRID with 1 mm beamlet spacing (this experiment). (b) Relative dose map for 20x20 mm<sup>2</sup> bar GRID with 1 mm beamlet spacing (Johnson *et al.*) [18]. (c) Relative dose map for 20x20 mm<sup>2</sup> bar GRID with 1.25 mm beamlet spacing (this experiment). (d) Relative dose map for 20x20 mm<sup>2</sup> bar GRID with 1.25 mm beamlet spacing (Johnson *et al.*).**

The relative dose maps for the bar GRIDs were considerably noisier than those measured in Johnson *et al.*, with less dose uniformity in the beamlets in the 1 mm beamlet spacing bar GRID dose map. The valley doses for the dose maps produced in this experiment appear comparable to those measured in Johnson *et*

*al.*—a notion which will be explored in section 3.3.3.1 with the dose volume histograms.

Inconsistencies between GRIDs measured in this experiment and those measured in Johnson *et al.* may be related to the uncertainty associated with EBT3 film measurements, with noise being a product of inhomogeneities in pixel intensity in each film. However, it may also be attributable to the use of the SARRP, which may have not only a different source size, but also certainly has different collimation than the XRAD 225Cx used in Johnson *et al.* (using the MVC as opposed to a conventional treatment cone)—consequently causing variations in both geometric and transmission penumbra.

These relative dose maps were further assessed by being converted into dose volume histograms for each GRID, as evidenced by Figure 29 and Figure 30 in section 3.3.2.1. Integral dose relative to open field for each GRID was also calculated in MATLAB using information from these dose maps, and was compared to the results in Johnson *et al.*

### **3.3.3.1 Dose Volume Histogram**

DVHs were produced using MATLAB and are represented in the plots in Figure 29 and 30:

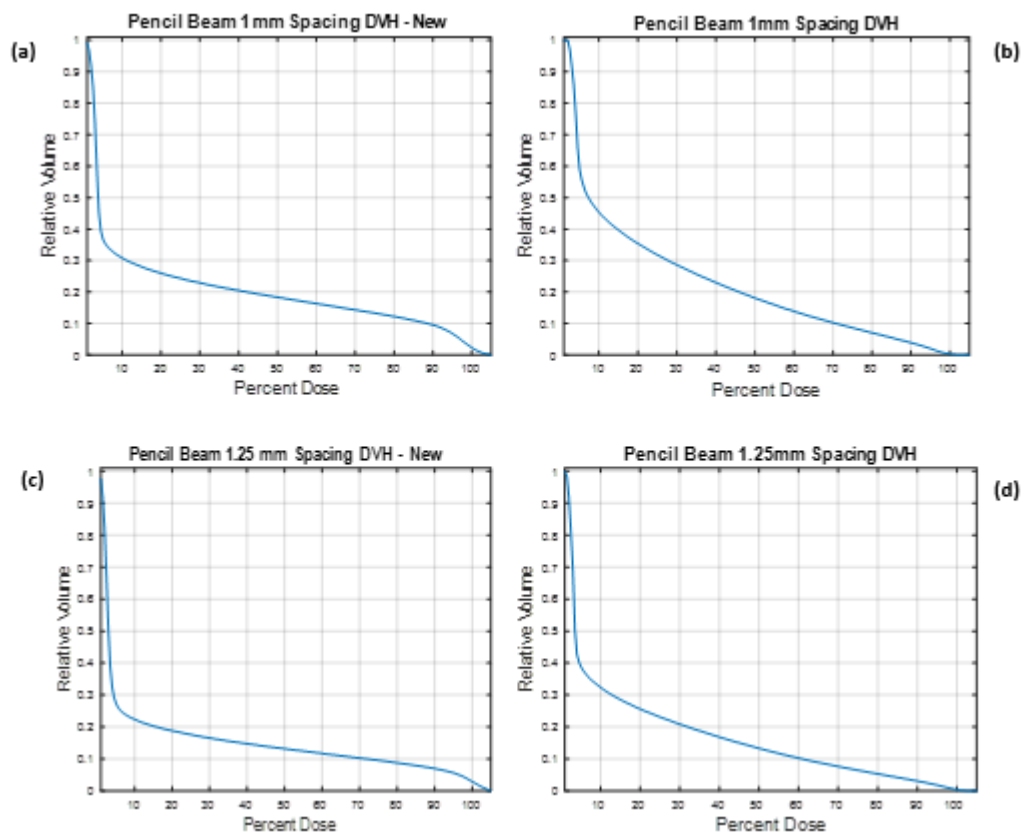


**Figure 29: (a) DVH for 20x20 mm<sup>2</sup> pencil GRID with 1 mm beamlet spacing (this experiment). (b) DVH for 20x20 mm<sup>2</sup> pencil GRID with 1 mm beamlet spacing (Johnson *et al.*) [18]. (c) DVH for 20x20 mm<sup>2</sup> pencil GRID with 1.25 mm beamlet spacing (this experiment). (d) DVH for 20x20 mm<sup>2</sup> pencil GRID with 1.25 mm beamlet spacing (Johnson *et al.*).**

Some agreement was seen in the DVH trends for the 1 mm and 1.25 mm pencil GRIDs relative to those produced in Johnson *et al.*, with deviations in the amount of relative volume receiving less than 10% of the average peak dose for both GRIDs. Regarding the pencil beam with 1 mm beamlet spacing, approximately 70% of the treatment volume was receiving less than 10% of the average peak dose (< .5 Gy), compared to the results in Johnson *et al.*, which observed approximately 55% of the treatment volume receiving less than 10% of the average peak dose.

Similarly, approximately 80% of the treatment volume was receiving less than 10% of the average peak dose for the 1.25 mm spacing pencil GRID, compared to 70% of the relative volume receiving less than 10% of the average peak dose for the same GRID in Johnson *et al.* That said, the DVHs for both pencil GRIDs also indicate that 2.9% and 4.2% of the relative volume was receiving the prescription dose for the 1 mm and 1.25 mm beamlet spacing pencil GRIDs, respectively, which is considerably higher than the findings in Johnson *et al.* (.45% and .43% for the same GRIDs). [18].

The 50% lymphocyte sparing dose threshold is approximately 1.5 Gy, and was used to evaluate the DVHs produced in this experiment relative to those created in Johnson *et al.* using the XRAD 225Cx. Assuming a prescription dose of 15 Gy (as in Johnson *et al.*), the amount of the treatment volume receiving less than 1.5 Gy was measured in MATLAB to be approximately 68.8% and 77.6% for the 1 mm and 1.25 mm pencil GRIDs, respectively, compared to 54% and 67% for the same GRIDs in Johnson *et al.* This corroborates the analysis of the DVHs in Figure 29, suggesting that more theoretical lymphocytes would have been spared with treatment using the SARRP.

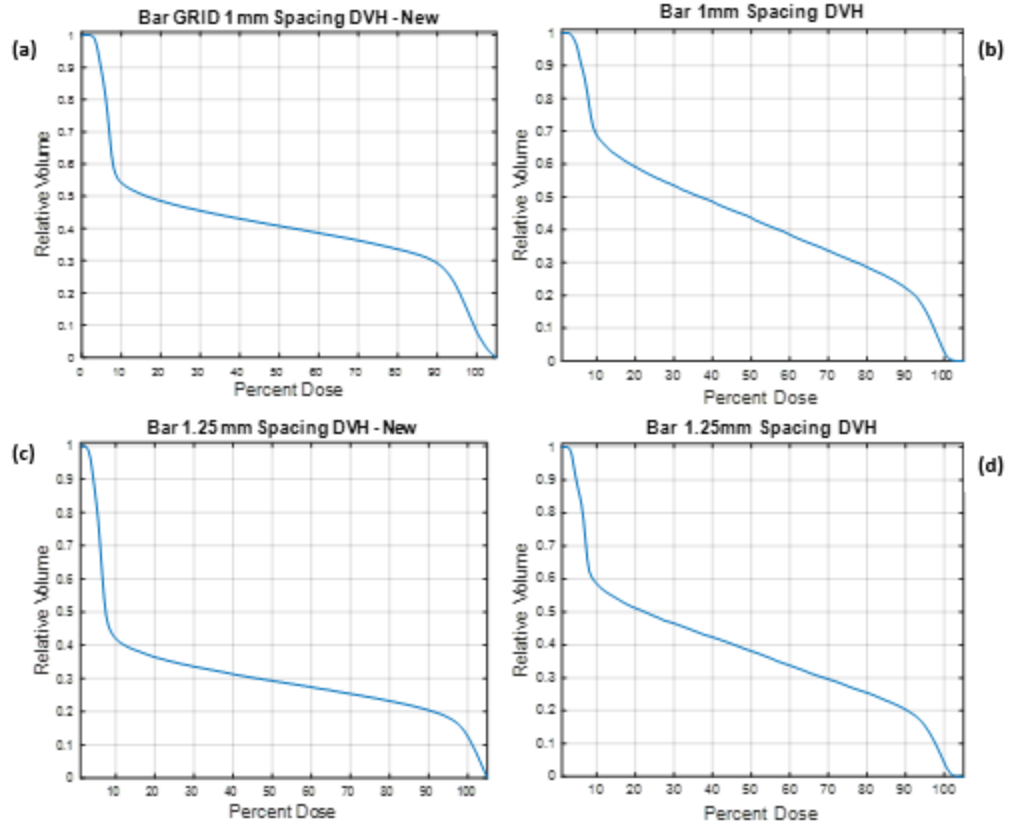


**Figure 30: (a) DVH for 20x20 mm<sup>2</sup> bar GRID with 1 mm beamlet spacing (this experiment). (b) DVH for 20x20 mm<sup>2</sup> bar GRID with 1 mm beamlet spacing (Johnson *et al.*) [18]. (c) DVH for 20x20 mm<sup>2</sup> bar GRID with 1.25 mm beamlet spacing (this experiment). (d) DVH for 20x20 mm<sup>2</sup> bar GRID with 1.25 mm beamlet spacing (Johnson *et al.*).**

The bar GRID DVHs measured in this experiment did not fully corroborate the DVHs for the same GRIDs generated in Johnson *et al.* The percent of the treatment volume receiving less than 10% of the average peak dose was roughly 45% for the 1 mm beamlet spacing bar GRID, and 60% for the 1.25 mm beamlet spacing bar GRID characterized using the SARRP, compared to approximately 30% and 40% of the treatment volume receiving less than 10% of the average peak dose in Johnson *et al.*

As with the pencil GRIDs, in-house MATLAB code was used to calculate what percentage of the treatment volume received less than 1.5 Gy (assuming 15 Gy prescription dose) for both bar GRIDs. These values were 44.3% and 51.4% for the 1 mm and 1.25 mm beamlet spacing bar GRIDs, respectively, compared to 31.0% and 40.1% for the same GRIDs in Johnson *et al.* This corroborates the initial analysis of the DVHs. Consequently, as with the characterized pencil GRIDs, more theoretical lymphocytes would have been spared in this experiment using the SARRP than with the XRAD 225Cx.

### 3.3.3.2 Integral Dose Relative to Open Field

Using in-house MATLAB code, the values for integral dose relative to open field measured in this experiment for the 20 x 20 mm<sup>2</sup> pencil and bar GRIDs are depicted in Table 17, and compared to the values produced in Johnson *et al.* via calculation of percent difference:

**Table 17: Comparison of experimental integral dose relative to open field measured for the 20x20 mm<sup>2</sup> pencil and bar GRIDs (1 mm and 1.25 mm beamlet spacing measured on April 11th, 2022, using the SARRP) with integral dose relative to open field values measured for the same GRIDs using the XRAD 225Cx in Johnson *et al* [18].**

Grid Type	Integral Dose Relative to Open Field (SARRP)	Integral Dose Relative to Open Field (XRAD 225Cx)	Percent Difference (%)
Pencil GRID, 1 mm beamlet spacing	21.8% ± 0.2	23.9% ± 0.3	-2.10
Pencil GRID, 1.25 mm beamlet spacing	16.9% ± 0.5	17.9% ± 0.1	-1.00
Bar GRID, 1 mm beamlet spacing	44.6% ± 0.1	45.9% ± 0.4	-1.30
Bar GRID, 1.25 mm beamlet spacing	40.4% ± 0.4	41.4% ± 0.4	-1.00

Higher integral dose was observed for all GRIDs characterized in Johnson *et al.* relative to those in this experiment—outside of the standard deviation for each measurement. However, all integral dose values were measured to be similar to those measured in Johnson *et al.* (1% to 2.1% difference), suggesting that the cumulative dose delivered to the EBT3 films used was effectively the same using the SARRP and XRAD 225Cx.

## **4. Conclusions**

### **4.1 *Verifying Xstrahl Factory Commissioning Results***

Verification of the Xstrahl factory commissioning results using a farmer ion chamber revealed that the data provided by the manufacturer was reliable and applicable to subsequent experiments. The measured TG-61 output, 3.66 Gy/min, aligned exactly with the nominal TG-61 output provided by Xstrahl. Similarly, the measured half-value layer was .66 mm Cu, which was ultimately only 1.5% different than the Xstrahl measured half-value layer of .67 mm Cu.

The reproducibility of these core measurements regarding beam quality and output add to the validity of the verification measurements for the PDC, as well as the reputability of the GRID characterizations using the SARRP.

### **4.2 *Verifying the Accuracy of the MuriPlan Integrated Point Dose Calculator***

As a contrast to the consistency between the factory commissioning results and the experimental commissioning measurements conducted in this thesis, verification of the MuriPlan PDC contained significant deviations from predicted values. EBT3 film dosimetry proved to be a relatively unreliable measure of the accuracy of the PDC. With film measured doses demonstrating percent differences ranging from 0.20% to 25% from PDC-predicted doses, and no observable trends suggesting a single reason for these differences, it became difficult to affirm the reliability of PDC-calculated exposure times for future preclinical experimentation.

At a minimum, it was evident that EBT3 film results alone would not be sufficient to verify the accuracy of the PDC.

Use of the MOSFET detectors, in addition to MuriPlan treatment planning simulations, provided sufficient evidence that the inconsistent EBT3 film results were anomalous, and do not invalidate the effectiveness of the PDC for treatment planning purposes. The MOSFET detector measurements demonstrated consistent agreement with the PDC-predicted dose, with 7/8 measurements being between .12% and 6%. Only a single measurement—the 10 x 20 mm<sup>2</sup> field—rose to the level of 18% difference from the predicted value, which was likely a function of user error.

With the addition of MuriPlan simulations generating dose delivery predictions more consistently close to the PDC-predicted dose than the EBT3 film results, it became clear that the PDC is an effective tool for calculating the exposure time necessary to deliver the operator-inputted dose for a particular depth and MVC field size. For the purposes of this thesis, the effectiveness of the PDC also translated as a reliable method for determining the exposure time for administering 6 Gy to the surface film used for mini-GRID characterizations.

### **4.3 GRID Characterizations**

Higher peak:valley ratios for pencil GRIDs with equivalent beamlet spacing were measured relative to characterized bar GRIDs in this experiment. Peak:valley ratios increased with increasing beamlet spacing for both pencil ( $24.5 \pm 0.6$  to  $25.1 \pm 1.3$ ) and bar ( $13.2 \pm 1.1$  to  $18.5 \pm 1.2$ ) GRIDs, suggesting that scatter from the

primary beam was mitigated with the addition of more attenuating material between each beamlet.

Higher output factors were measured for bar GRIDs relative to pencil GRIDs (equivalent beamlet spacing), with output factors decreasing with respect to increasing beamlet spacing for both GRID types. For the pencil GRIDs, output factors were determined to be  $.77 \pm .03$  and  $.74 \pm .02$  (1 mm and 1.25 mm beamlet spacing, respectively). The 1 mm and 1.25 mm bar GRIDs had output factors of  $.83 \pm .03$  and  $.80 \pm .03$ , respectively.

For each GRID type, output factor decreases with decreased percent area treated; as such, it makes sense that the bar GRIDs would have higher output factors relative to the pencil GRIDs, with the 1 mm beamlet spacing bar GRID having the highest percent area treated (50%) and consequently the highest output factor [18].

The results of the mini-GRID characterizations in this experiment corroborate the mini-GRID characterization trends in Johnson *et al.*, despite not mirroring the precise results for a majority of the peak:valley ratios and for the bar GRID output factors. It is plausible that discrepancies in measurements are a result of using different technology (rather, the new installation of the SARRP). As such, with more GRID characterization trials, it is likely that percent differences can be minimized, or at least resolved as being consistent with the feature differences of the SARRP relative to the XRAD 225Cx.

The setup from the XRAD 225Cx used for GRID characterizations in Johnson *et al.* was demonstrated to be reproducible using the SARRP. With the addition of

CBCT on-board imaging, isocenter localization and dose delivery precision are improved on the SARRP relative to the XRAD 225Cx. Moving forward, while additional GRID characterizations will need to be completed to verify the reproducibility of the results in Johnson *et al.* — as well as to inform the experimental plan for a future preclinical mouse trial evaluating mini-GRID treatment efficacy — this thesis demonstrates that the SARRP has similar, if not improved, mini-GRID characterization and treatment capabilities compared to the previously installed XRAD 225Cx.

#### **4.4 Future Study**

The capabilities of the Xstrahl SARRP for mini-GRID characterization and treatment has implications for future study. Referring to the results of the preclinical mouse experiment in Johnson *et al.*, a 15 Gy treatment using the bar GRID (1 mm beamlet spacing) proved to have significantly inferior tumor control relative to 15 Gy administered via conventional radiation therapy [18]. This mouse experiment was a novel insofar as no other study had tested GRID therapy efficacy as a standalone procedure compared to conventional treatment efficacy. While the results of Johnson *et al.* illustrated that for the same dose and single fraction conventional therapy is superior, further study remains necessary investigating the utility of GRID therapy coupled with a PD-L1 checkpoint blockade, or as a treatment delivered in multiple fractions. Perhaps most promisingly is the combination of GRID therapy and immunotherapy — with the immunotherapy component being the aforementioned PD-L1 checkpoint inhibition drug.

A potential study to evaluate this treatment approach would involve four primary treatment arms, including an unirradiated control; a group receiving mini-GRID therapy coupled with a PD-L1 checkpoint inhibition drug; a group receiving mini-GRID therapy without a PD-L1 checkpoint inhibitor; and, finally, a group designated to receive conventional radiation therapy (or full irradiation). Each group would consist of approximately 15 mice C57BL/6 mice, transplanted with a p53/MCA sarcoma model, as was utilized in Johnson *et al.* The mini-GRID utilized would likely be a pencil GRID, due to its characteristically high peak-to-valley ratio and consequent ability to deliver high doses to specific portions of the mouse tumor, while concurrently achieving low valley doses (less than 1.5 Gy) in the effort of sparing lymphocytes.

## References

- (1) Xstrahl Life Sciences. (2017). *SARRP Pro 4D Technical Description*. Xstrahl Life Sciences. <https://duke.app.box.com/file/843370734848?sb=/activity>
- (2) Spolar, M. (2021, November 29). *Installs 100th 3D Cabinet Irradiator*. Xstrahl. <https://xstrahl.com/100irradiator/>
- (3) Goetz, Wilfried, Tryggestad E. (2020). *SARRP Dosimetric Commissioning*. Xstrahl Life Sciences. <https://duke.app.box.com/file/843366421243>
- (4) Johnstone, C. D., Lindsay, P., Graves, E. E., Wong, E., Perez, J. R., Poirier, Y., Ben-Bouchta, Y., Kanesalingam, T., Chen, H., Rubinstein, A. E., Sheng, K., & Bazalova-Carter, M. (2017). *Multi-institutional MicroCT image comparison of image-guided small animal irradiators*. *Physics in Medicine & Biology*, 62(14), 5760–5776. <https://doi.org/10.1088/1361-6560/aa76b4>
- (5) Yan, W., Khan, M. K., Wu, X., Simone, C. B., 2nd, Fan, J., Gressen, E., Zhang, X., Limoli, C. L., Bahig, H., Tubin, S., & Mourad, W. F. (2019). *Spatially fractionated radiation therapy: History, present and the future*. *Clinical and translational radiation oncology*, 20, 30–38. <https://doi.org/10.1016/j.ctro.2019.10.004>
- (6) Griffin, Robert J., Mansoor M. Ahmed, Beatriz Amendola, Oleg Belyakov, Søren M. Bentzen, Karl T. Butterworth, Sha Chang, et al. *Understanding High-Dose, Ultra-High Dose-Rate and, Spatially Fractionated Radiotherapy*. *International Journal of Radiation Oncology\*Biophysics\*Physics*, April 13, 2020. <https://doi.org/10.1016/j.ijrobp.2020.03.028>.
- (7) Rivera JN, Kierski TM, Kasoji SK, Abrantes AS, Dayton PA, et al. (2020) *Conventional dose rate spatially-fractionated radiation therapy (SFRT) treatment response and its association with dosimetric parameters — A preclinical study in a Fischer 344 rat model*. *PLOS ONE* 15(6): e0229053. <https://doi.org/10.1371/journal.pone.0229053>

- (8) Sathishkumar S., Dey S., Meigooni A.S. *The impact of TNF-alpha induction on therapeutic efficacy following high dose spatially fractionated (GRID) radiation*. Technol Cancer Res Treat. 2002 Apr;1(2):141–147
- (9) Najafi, M., Fardid, R., Hadadi, G., & Fardid, M. (2014). *The mechanisms of radiation-induced bystander effect*. Journal of biomedical physics & engineering, 4(4), 163–172.
- (10) Asur RS, Sharma S, Chang CW, Penagaricano J, Kommuru IM, Moros EG, Corry PM, Griffin RJ. *Spatially fractionated radiation induces cytotoxicity and changes in gene expression in bystander and radiation adjacent murine carcinoma cells*. Radiat Res. 2012 Jun;177(6):751-65. doi: 10.1667/rr2780.1. Epub 2012 May 4. PMID: 22559204; PMCID: PMC3395590.
- (11) Tubin, Slavisa, Helmut H. Popper, and Luka Brcic. *Novel Stereotactic Body Radiation Therapy (SBRT)-Based Partial Tumor Irradiation Targeting Hypoxic Segment of Bulky Tumors (SBRT-PATHY): Improvement of the Radiotherapy Outcome by Exploiting the Bystander and Abscopal Effects*. Radiation Oncology 14, no. 1 (January 29, 2019): 21. <https://doi.org/10.1186/s13014-019-1227-y>.
- (12) Herrera FG, Bourhis J, Coukos G. *Radiotherapy combination opportunities leveraging immunity for the next oncology practice*. CA Cancer J Clin. 2017 Jan;67(1):65-85. doi: 10.3322/caac.21358. Epub 2016 Aug 29. PMID: 27570942.
- (13) Markovsky, Ela, Sadna Budhu, Robert M. Samstein, Hongyan Li, James Russell, Zhigang Zhang, Esther Drill, et al. *An Antitumor Immune Response Is Evoked by Partial-Volume Single-Dose Radiation in 2 Murine Models*. International Journal of Radiation Oncology\*Biophysics\*Physics, no. 3 (March 1, 2019): 697–708. <https://doi.org/10.1016/j.ijrobp.2018.10.009>.
- (14) Sammer M, Teiluf K, Girst S, Greubel C, Reindl J, et al. (2019) *Beam size limit for pencil minibeam radiotherapy determined from side effects in an in-vivo mouse ear model*. PLOS ONE 14(9): e0221454. <https://doi.org/10.1371/journal.pone.0221454>

- (15) Mohiuddin M, Fujita M, Regine WF, et al. *High-dose spatially-fractionated radiation (grid): A new paradigm in the management of advanced cancers*. Int J Radiat Oncol Biol Phys 1999;45:721-7.
- (16) Buckey, Courtney, Sotirios Stathakis, Ken Cashon, Alonso Gutierrez, Carlos Esquivel, Chengyu Shi, and Nikos Papanikolaou. *Evaluation of a Commercially-Available Block for Spatially Fractionated Radiation Therapy*. Journal of Applied Clinical Medical Physics 11, no. 3 (June 2010): 2–11.  
<https://doi.org/10.1120/jacmp.v11i3.3163>.
- (17) Wu X, Ahmed M, Wright J, et al. *On Modern Technical Approaches of Three-Dimensional High-Dose Lattice Radiotherapy (LRT)*. Cureus 2(3): e9.
- (18) Johnson TR, Bassil AM, Williams NT, Brundage S, Kent CL, Palmer G, Mowery YM, Oldham M. *An investigation of kV mini-GRID spatially fractionated radiation therapy: dosimetry and preclinical trial*. Phys Med Biol. 2022 Feb 18;67(4). doi: 10.1088/1361-6560/ac508c. PMID: 35100573.
- (19) Sorriaux J, et al., *Evaluation of Gafchromic EBT3 films characteristics in therapy photon, electron and proton beams*. Physica Medica (2012),  
<http://dx.doi.org/10.1016/j.ejmp.2012.10.001>
- (20) GAFCHROMIC DOSIMETRY MEDIA, TYPE EBT-3. (n.d.).  
[http://www.gafchromic.com/documents/EBT3\\_Specifications.pdf](http://www.gafchromic.com/documents/EBT3_Specifications.pdf)
- (21) Newton J, Oldham M, Thomas A, Li Y, Adamovics J, Kirsch DG, Das S. *Commissioning a small-field biological irradiator using point, 2D, and 3D dosimetry techniques*. Med Phys. 2011 Dec;38(12):6754-62. doi: 10.1118/1.3663675. PMID: 22149857; PMCID: PMC3247930.
- (22) Oncology medical physics. Oncology Medical Physics. (n.d.). Retrieved March 6, 2022, from <https://oncologymedicalphysics.com/mosfet-detectors/>

- (23) Kim, S. W., Shin, H. J., Kay, C. S., & Son, S. H. (2014). *A customized bolus produced using a 3-dimensional printer for radiotherapy*. PloS one, 9(10), e110746. <https://doi.org/10.1371/journal.pone.0110746>
- (24) Bazyar, Soha, Christina R Inscoe, E Timothy O'Brian, Otto Zhou, and Yueh Z Lee. *Minibeam Radiotherapy with Small Animal Irradiators; in Vitro and in Vivo Feasibility Studies*. *Physics in Medicine & Biology* 62, no. 23 (November 10, 2017): 8924–42. <https://doi.org/10.1088/1361-6560/aa926b>.
- (25) Drzymala, R. E., Mohan, R., Brewster, L., Chu, J., Goitein, M., Harms, W., & Urie, M. (1991). *Dose-volume histograms*. *International journal of radiation oncology, biology, physics*, 21(1), 71–78. [https://doi.org/10.1016/0360-3016\(91\)90168-4](https://doi.org/10.1016/0360-3016(91)90168-4)